Profiled bar transmission gratings: soft x-ray calibration of new Kirchoff solutions

Michael C. Hettrick, Michael E. Cuneo, John L. Porter, Larry E. Ruggles, Walter W. Simpson, Mark F. Vargas, and David F. Wenger

Applied Optics Vol. 43, Issue 19, pp. 3772-3796 (2004)

http://dx.doi.org/10.1364/AO.43.003772

also see erratum at:

Applied Optics Vol. 43, Issue 25, pp. 4785-4785 (2004)

http://dx.doi.org/10.1364/AO.43.004785

Profiled bar transmission gratings: soft-x-ray calibration of new Kirchoff solutions

Michael C. Hettrick, Michael E. Cuneo, John L. Porter, Larry E. Ruggles, Walter W. Simpson, Mark F. Vargas, and David F. Wenger

A new analytical model, derived rigorously from scalar diffraction theory, accurately fits soft-x-ray measurements of symmetrical profile gold transmission gratings in all diffracted orders. The calibration system selects numerous photon energies by use of a high-resolution grazing-incidence monochromator and a dc *e*-beam source. Fine-period free-standing gratings exhibit limited performance and require such testing to determine parameters of and select acceptable gratings for use in time-resolved (0.25 ns) spectrographs of known radiometric response. Unfolded spectra yield a *Z*-pinch plasma peak kT ~250 eV, total radiated energy ~900 kJ, and a pinch-driven gold-wall hohlraum Planckian kT ~86 eV.

OCIS codes: 050.1950, 050.1960, 300.6560.

1. Introduction

Transmission gratings can play a useful role in soft-x-ray spectroscopy. Although their dispersive power and peak efficiency are generally lower than those of grazing-incidence reflection gratings, transmission gratings have a broad range of spectral coverage and can, in principle, exhibit low contamination from undesired (usually $m = 2$) spectral orders.

The physical model of a classical rectangular bar transmission grating has been previously solved in closed form,[1] yielding a relative efficiency in the nonzero orders m of

$$\eta_m = [\sin(m\pi a/d)/(m\pi)]^2(1 + c_1{}^2 - 2c_1c_2) \quad (1)$$

and a zero-order relative efficiency of

$$\eta_0 = (a/d)^2 + [1 - (a/d)]^2c_1{}^2 + 2(a/d)[1 - (a/d)]c_1c_2, \quad (2)$$

where the efficiencies are relative to the transmission of any structure supporting the grating, d is the grating period, a is the gap between the bars, and where the wavelength-dependent terms c_1 and c_2 are

$$c_1 = \exp(-2\pi\beta z_o/\lambda), \quad (3)$$

$$c_2 = \cos(2\pi\delta z_o/\lambda), \quad (4)$$

for a bar of thickness z_o composed of material having a complex refractive index $\mathbf{n} = (1 - \delta) + i\beta$ at a wavelength $\lambda = hc/E$, where E is the photon energy, h is Planck's constant, and c is the speed of light in vacuo. In convenient units, λ (Å) = $12398.5/E$(eV).

This simple model has been widely accepted and used to approximate the efficiency of transmission gratings for various applications in space astronomy and laboratory sciences.[1–4] However, from Eq. (1) the rectangular bar model is seen to result in a ratio of efficiencies in nonzero order p to the first order ($m = 1$) which is independent of wavelength

$$\eta_p/\eta_1 = [(1/p)\sin(p\pi a/d)/\sin(\pi a/d)]^2. \quad (5)$$

Although none of the soft-x-ray transmission gratings reported in the referenced literature display such a precisely constant ratio of efficiencies, the numerical deviations were usually tolerable. This is because such gratings had a/d ratios significantly less than 0.50. However, the newest gratings to be calibrated in the present work have a/d values approaching 0.50, which Eq. (5) shows to result in η_p/η_1 approaching zero for even orders p. This condition is ideal for removing spectral contam-

M. C. Hettrick (hettrickscientific@yahoo.com) is with Hettrick Scientific, 1-39-59 Tama-cho, Fuchu-shi, Tokyo, Japan 183-0002. M. E. Cuneo, J. L. Porter, L. E. Ruggles, W. W. Simpson, M. F. Vargas, and D. F. Wenger are with Sandia National Laboratories, Albuquerque, New Mexico 87185-1193.

Received 25 September 2003; revised manuscript received 30 March 2004; accepted 5 April 2004.

0003-6935/04/193772-25$15.00/0

ination from the even orders, especially $m = 2$. However, because of wavelength-dependent transmission through the sloped sidewalls of nonrectangular grating bars, the deviation from a constant efficiency ratio becomes more pronounced for such gratings, since the percentage change in second-order efficiency becomes sensitive to small changes in the effective value of a/d as a function of wavelength.

Furthermore, the level of accuracy required for proper calibration of the gratings for our applications is higher than has been considered acceptable in the past. Our goal here was to measure and model gold-bar transmission gratings to an absolute accuracy better than 5% of the first-order efficiency integrated over the spectrum of a *Z*-pinch or pinch-driven hohlraum source (~0.1–2 KeV). A similar 5% requirement is imposed on the absolute calibration of the pin silicon photodiodes used to record the spectrum and is discussed briefly in Subsection 6.A. Such high accuracy is for the purpose of providing transmission grating spectrometer (TGS) instruments capable of measuring these sources to the level required for fusion energy diagnostics. Such sources are spectral continua of otherwise uncalibrated intensity and thus lack the characteristics that can provide any *in situ* calibration capability often available to astronomical or synchrotron instrumentation. Furthermore, our transmission gratings can be heated to near the melting point of the bar material, as they are oriented at normal incidence to the highest peak power soft-x-ray pulse in existence (the Sandia National Laboratories *Z* pinch), and hence must be fully calibrated both prior to and periodically during their use in the spectrometers. Therefore, a (table-top) calibration system must be available and nearby the *Z*-accelerator facility.

In this study, we have therefore endeavored both to improve the accuracy of absolute efficiency measurements on soft-x-ray (free-standing) transmission gratings and to develop correspondingly more accurate efficiency models through the closed-form derivation of new equations using scalar diffraction theory. Section 2 describes the table-top calibration system we developed for this study. Such calibration must have high enough spectral resolution to monitor the photoabsorption edges that provide an accurate way to determine the thicknesses and coverage of translucent support structures and contaminants and must also provide the spatial resolution needed to characterize variations in efficiency across the usable aperture of the grating. Section 3 presents the new equations for efficiencies of nonrectangular bar shapes, including both linear (e.g., trapezoidal and hexagonal) and nonlinear thickness profiles. These equations are derived in exact form with Kirchoff's method of complex secondary wave summation, rather than being numerical or other partially formulated approximations adapted from the equations of a rectangular bar.[2,4,5] Section 4 addresses practical aspects of calibrating the grating efficiency, including sources of measurement error, grating support structures, contamination, scattering, and spatial variations. Section 5 presents the calibrated data fits for a number of gratings with different periods and over several generations of manufacture. The model fits use a new computer code developed to efficiently search for the multidimensional physical parameters of the grating that best fit the data in a physically robust manner. Section 6 presents absolutely calibrated scientific results from the *Z* accelerator by time-resolved spectrographs constructed from two gratings selected for their comparatively high-performance characteristics. Section 7 summarizes this study, including observations on the structural and performance limitations of the transmission gratings obtained in this research.

2. Calibration System

The soft-x-ray light source was a Manson Model 2 electron impact device manufactured by Austin Instruments, Inc.[6] It provides a generally stable source of soft x rays and is typically outfitted with a handful of anodes that produce strong *K*-shell emission lines (Al, Mg, O, C, B, and Be). As the current calibration effort mandated mapping absorption edges and efficiency variations requiring several dozen photon energies, numerous anode materials were tested. This testing culminated in a set of 24 solid anodes (Hettrick Scientific Model CAL-24 custom anode library[7]) that deliver approximately 75 usable emission lines in the soft-x-ray region (Table 1). The spatial and temporal stability of the source was also improved significantly by addition of a copper block radiator and by fan cooling of the anode.

Two monochromators were used to select the desired photon energy: a moderate-dispersion model SNR-I and a high-dispersion model SXR-II, both manufactured by Hettrick Scientific.[7] The lower-resolution instrument is a compact astigmatic configuration (Fig. 1) that selects photon energy through rotation of a concave grating about its surface normal,[8,9] whereas the higher-resolution instrument (Fig. 2) is a stigmatic configuration that employs varied-line-space (VLS) reflection gratings.[10] Both monochromators provide high throughput combined with a fixed position source and exit slit. The mechanical stability afforded by this robust (fixed-slit) configuration allowed long-duration constant-intensity exposures at the designed spectral resolution. For maximum throughput, the source functioned as the object point of the monochromator in lieu of an entrance slit. For minimal undesirable contamination from visible–UV radiation and from overlapping spectral orders of the monochromator, a selection of thin-film filters manufactured by LeBow Company[11] was placed between the source and the monochromator, as tabulated in Table 1. Photon energies $E \geq 1380$ eV use the second order from the monochromator, with the filter chosen to minimize the unwanted first-order throughput at photon energy $E/2$.

Table 1. Electron Impact Source Anode Lines

eV	Species	[a]Filter
49.3	Mg–L/M	
72.4	Al–L/M	
91.5	Si–L/M	
108.5	Be–Ka	Zr (0.2)
132.8	Y–Mz	Zr (0.2)
151.1	Zr–Mz	Zr (0.2)
171.7	Nb–Mz	Zr (0.2)
183.3	B–Ka	Zr (0.2)
192.6	Mo–Mz	Zr (0.2)
237	Ru–Mz	C (1.0)
260	Rh–Mz	
277	C–Ka	C (1.0)
284.4	Pd–Mz	None
311.7	Ag–Mz	Ti (0.3)
395.3	Ti–Ll	Ti (0.3)
397	Sn–Mz	
401.3	Ti–Le	
446.5	V–Ll	
452.2	Ti–La	Ti (0.3)
453.5	V–Le	
458.4	Ti–Lb	
500.3	Cr–Ll	None
510.2	Cr–Le	
511.3	V–La	
519.2	V–Lb	
524.9	[b]O–Ka	None
572.8	Cr–La	Ni (0.3)
582.8	Cr–Lb	
615.2	Fe–Ll	Co (0.5)
628	Fe–Le	
677.8	Co–Ll	Ni (0.3)
694	Co–Le	
705	Fe–La	Co (0.5)
718.5	Fe–Lb	
742.7	Ni–Ll	Ni (0.3)
762	Ni–Le	
776.2	Co–La	Ni (0.3)
791.4	Co–Lb	
811.1	Cu–Ll	Ni (0.3)
832	Cu–Le	Ni (0.3)
851.5	Ni–La	Ni (0.3)
868.8	Ni–Lb	Mg (10)
884	Zn–Ll	Mg (10)
929.7	Cu–La	Mg (10)
949.8	Cu–Lb	
1011.7	Zn–La	Mg (10)
1034.7	Zn–Lb	
1036.2	Ge–Ll	
1068	Ge–Le	Mg (10)
1188	Ge–La	Mg (10)
1218.5	Ge–Lb	
1253.6	Mg–Ka	Mg (10)
1302.2	Mg–Kb	
1380	W–Mz	Al (5)
1486.7	[b]Al–Ka	Al (5)
1557.5	[b]Al–Kb	Al (5)
1660.5	Au–Mz	
1685.4	Y–Ll	
1740	Si–Ka	Co (0.5)
1774	W–Ma	Co (0.5)
1761	Y–Le	
1792	Zr–Ll	
1835.9	Si–Kb	Co (0.5)
1876.5	Zr–Le	
1902.2	Nb–Ll	
1922.6	Y–La	Co(0.5)
1996.2	Nb–Le	
2015.7	Mo–Ll	
2042.4	Zr–La	Co(0.5)
2122.9	Au–Ma	
2165.9	Nb–La	Co(0.5)
2253	Ru–Ll	
2293.2	Mo–La	
2376	Rh–Ll	
2559	Ru–La	
2697	Rh–La	
2839	Pd–La	
2984	Ag–La	
3444	Sn–La	
4511	Ti–Ka	
4952	V–Ka	
5415	Cr–Ka	
6404	Fe–Ka	
6930	Co–Ka	
7478	Ni–Ka	
8048	Cu–Ka	
8639	Zn–Ka	
9887	Ge–Ka	

[a]Filter thickness (in micrometers) listed for lines used in this study.
[b]Line produced by a sapphire anode.

The transmission grating to be calibrated was placed at the exit slit plane of the monochromator. A reference exit slit of identical width and length as the slit preceding the transmission grating was alternately translated into the beam to provide absolute calibration of the transmission grating efficiency. The spectral orders of the monochromatic light dispersed by the transmission grating were imaged by a 20-μm pixel (1300 × 1340 format) Roper Scientific[12] Model PI-SX1300(B) back-illuminated thermoelectri-

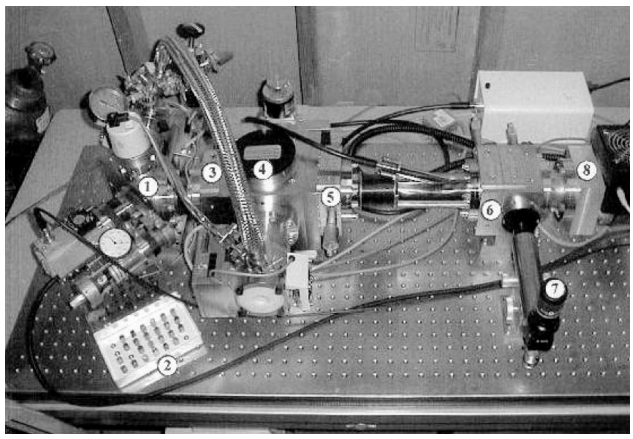

Fig. 1. Photograph of calibration system based on the moderate-resolution SNR monochromator: 1, Manson source; 2, custom-anode library; 3, aperture selector; 4, grazing-incidence monochromator grating; 5, filter selection; 6, exit slit or transmission grating; 7, *in situ* microscope; 8, CCD.

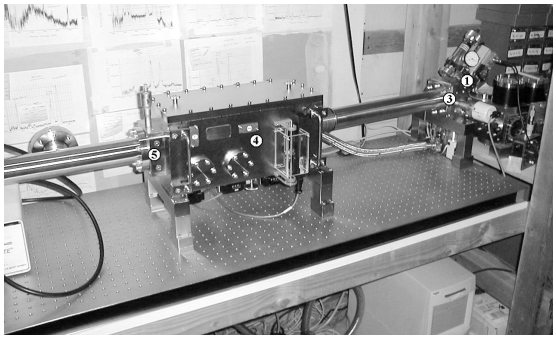

Fig. 2. Photograph of calibration system based on the high-resolution SXR monochromator. 1, Manson source; 3, filter selector; 4, grazing-incidence monochromator; 5, aperture selector. Exit slit or transmission grating, microscope, and CCD are off the photograph but are the same as shown in Fig. 1.

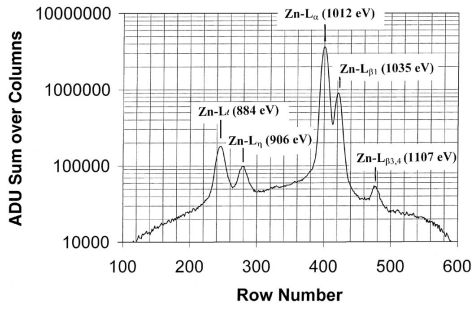

Fig. 3. Typical anode spectrum (zinc, 10 keV, 200 mA, Mg filter), showing three usable lines and a Bremsstrahlung continuum.

cally cooled CCD (EEV 36-40 chip), which had a low dark current (~0.2 e-/s/pixel at −60 °C) and excellent thermostatic precision (±0.05 °C). This detector replaced an older 24-μm pixel (1024 × 1024 format) Photometrics CCD (SITE chip) having significantly higher dark current (~11 e-/s/pixel at −40 °C), which was used for the first few grating calibrations. The CCD imaging surface was placed ~193 mm from the transmission grating to be calibrated. We obtained confirmation of the photon energy selected by the monochromator by first calibrating the dispersion scale of the transmission grating–CCD configuration using several orders of known narrow lines (e.g., Al–Kα at 1486.7 eV). The gratings tested in this study were free-standing transmission gratings fabricated by MIT Space Nanostructures Laboratory[13] and by Heidenhain GmbH.[14]

Figure 3 shows a typical anode spectrum, recorded with the SXR monochromator in spectrograph mode. In this mode, the CCD is placed at the monochromator image plane instead of the exit slit used during the calibrations. In this example, a zinc anode was used in the Manson source, resulting in several intense lines superimposed on a Bremsstrahlung continuum. Visible light from the source filament was removed by use of a 10-μm-thick magnesium filter. To obtain an accurate efficiency measurement at each spectral line ($E = h\nu$), we also took an off-line image at a nearby photon energy ($E + \Delta E$) for both the dispersed grating spectrum and the reference beam and subtracted it from the online image. This subtraction largely removes the underlying continuum from the line radiation, resulting in a monochromatic image of high purity. As shown in Fig. 4, for three photon energies spanning the soft x ray, the profile of this image in the dispersion direction of the grating produces a monochromatic spectrum of the grating spectral orders.

Increasing the signal-to-noise (S/N) ratio while canceling the effects of any linear change in the intensity of the transmitted source intensity as a function of time (see Subsection 4.A), required that four online and four offline reference slit images be taken, together with two online and one offline grating images. The averages of these exposures were made and the absolute efficiency calculated as

$$\eta_m = (S_R/S_G) \times (\mathrm{GRAT}_m\_\mathrm{ON} - \mathrm{GRAT}_m\_\mathrm{OFF} - \mathrm{GRAT}_m\_\mathrm{BASE})/(\mathrm{SLIT\_ON} - \mathrm{SLIT\_OFF}), \quad (6)$$

where S_R is the width of the reference slit and S_G is the width of the grating aperture slit. In this equation, any prefix term denoted by GRAT_m is the average intensity in spectral order m (grating in the beam), and any prefix term denoted by SLIT is the average intensity in the incident beam (reference slit in the beam). The suffix term ON refers to measurements taken at the center of the spectral line, and OFF refers to measurements taken at some spectral distance off-center. The term GRAT_m_BASE is the baseline intensity of the local continuum in the dispersed profile (such as shown in Fig. 4), measured to both sides of the peak in spectral order m and averaged. Its subtraction further increases the spectral and order purity by largely removing any residual nonmonochromatic light as well as monochromatic light scattered by the test grating (see Subsection 4.B), both of which are contained in the continuum lying underneath the measured order. To provide the maximum S/N ratio, we averaged all terms in Eq. (6) over the number of CCD bins needed to fully enclose the spectral order image.

Because the real and the scattered continuum being subtracted is generally sloped, the higher-resolution monochromator provided better results because of a smaller value for ΔE. In this case, a typical value chosen for the off-line measurement was $\Delta E/E$ ~0.01–0.02, depending on the natural width of the source line used. This provided satisfactory results for the X-series gratings, which required comparatively large slit widths of ~150 μm owing to the low geometric transmission of their support structure. Hereafter, we denote this geometric fraction as the open-area-ratio, or OAR, of the grating. As is evidenced by the smoothness of the data and the accuracy of the model fits (see Table 2 below and Section 5), the off-line subtractions benefited further by the increased spectral

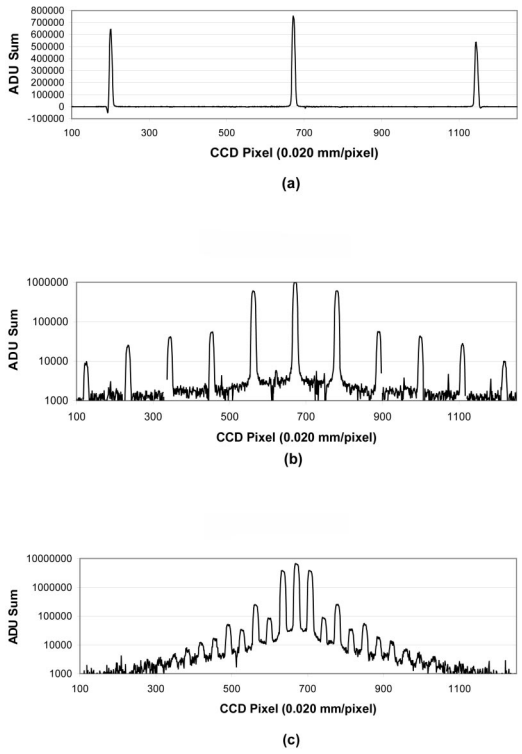

Fig. 4. Spectrum of monochromatic orders from grating HS14, at three sample photon energies. The CCD intercepts grating orders -1, 0, and $+1$ at (a) Y–Mζ (133 eV) and orders -5 to $+5$ at (b) Cr–Lα (573 eV). At (c) Si–Kα (1740 eV), grating orders -10 to $+10$ are detectable peaks above the scattered wings of the low-order profiles.

purity resulting from use of even narrower ($\sim$70 μm) width slits for the HS- and XS-series gratings, made possible by their higher OARs.

The moderate-resolution (SNR) monochromator was used only at the early stages of this study, for calibrating the HD6 and the FS-series gratings. For this monochromator, the separation between the on-line and the off-line settings was typically $\Delta E/E \sim 0.03$–0.10. In part, because of the sloped underlying higher-order and scattered continuum, the resulting subtraction from Eq. (6) resulted in marginal improvement compared with that of simply subtracting the detector background alone (turning off the anode potential). This simpler procedure was followed for calibration of the FS-series gratings. In this case, the residual higher orders and scattered radiation passing through the monochromator were not negligible effects in the resulting efficiencies and thus were subtracted when necessary by use of a bootstrap method in the data analysis (i.e., starting with the known uncontaminated efficiencies at the highest energies and then working one's way to the lower energies). However, this technique did not yield results as accurate as those from direct removal of such contamination with the higher-resolution monochromator.

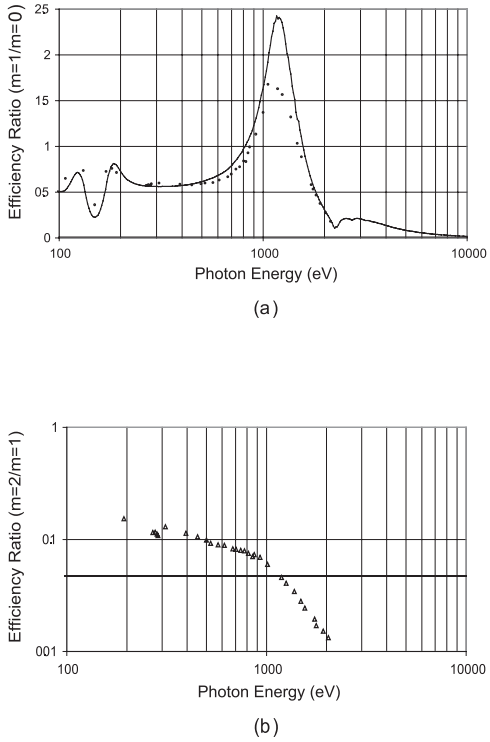

Fig. 5. HS14 efficiency ratio best fit of rectangular bar model (z_o = 275 nm, a/d = 0.430). (a) First-to-zero-order efficiency ratio. (b) Second-to-first-order efficiency ratio.

Figure 5 shows the conversion of the order spectra for grating HS14 to efficiency ratios, by use of Eq. (6). The smooth curves are the best fits of the classical bar model [Eqs. (1)–(5)], by use of a single set of physical parameters. It is evident from this result that the grating deviates significantly from a simple rectangular bar model. For example, the gap-to-period ratio (a/d) can be chosen to fit only the average value of η_2/η_1, resulting in a factor 5 overestimate to the measured results at the high-energy end and a factor 2 underestimate at the low-energy end. In addition, adjusting the gold-bar thickness (z_0) to fit the energy position of the peak in η_1/η_0 results in a peak magnitude that exceeds the measurements by nearly a factor of 2.

3. New Kirchoff Solutions

A. Linear Profile

Kirchoff scalar theory constructs the net electric field as the sum of all secondary waves from the diffracting surface. The efficiency is given by the modulus of the sum of the complex wave amplitudes. Identifying the four physically distinct regions of Fig. 6 for a grating bar with a thickness given by a trapezoidal figure, we have

$$\eta_m = [A_r(m) + B_r(m) + C_r(m) + D_r(m)]^2 + [A_i(m) + B_i(m) + C_i(m) + D_i(m)]^2, \quad (7)$$

where, for example, $\mathbf{A} = A_r + iA_i$ is the complex amplitude from region A.

The periodic grating structure diffracts the incident wave into discrete spectral orders, m, in accordance with the grating equation. The incident parallel wave front is assumed to travel in the vertical direction of Fig. 6. Changes in phase and amplitude are calculated as a function of the horizontal position with the complex refractive index and thickness of the bar along that vertical line-of-sight (l-o-s). Because this calculation assumes the wave does not change direction through grating diffraction until it arrives at a common vertical position after passing through the bars, the results are independent of the vertical position at which the phase and amplitude changes take place. Therefore, the linear variation of thickness that defines the side walls of this model is the result of any one of a series of hexagonal profiles (dashed outline) whose limited case is a trapezoidal profile (solid outline).

The derivation of the individual terms **A** through **D** involves the following steps:

1. Setting up the Kirchoff integrals, following the general formulation of Eidmann,[2]
2. Simplifying the integration by combining like terms into the four physically distinct regions (A, B, C, and D),
3. Performing the integration and separating the results into real and imaginary components,
4. Simplifying the expressions to permit physical insight and numerical calculation of the results.

Thereby, after significant algebraic manipulation in rigorous conformance with scalar diffraction theory and the procedure outlined in steps 1–4 above, the wave amplitude components for spectral orders m not equal to zero have been solved as

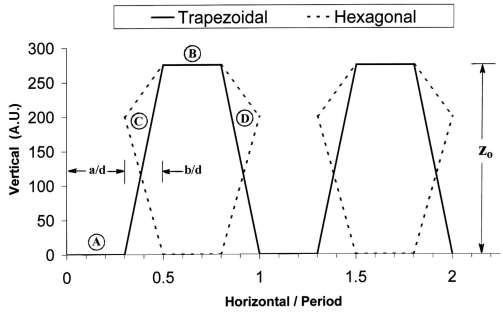

Fig. 6. Linear side-wall bar profile model.

where $\phi_a = 2\pi ma/d$ and $\phi_b = 2\pi mb/d$.

For $m = 0$, after precautions are taken to avoid indeterminate expressions, the wave amplitude components are given by

$$A_r(0) = a/d, \tag{16}$$

$$A_i(0) = 0, \tag{17}$$

$$B_r(0) = c_1c_2(1 - a/d - 2b/d), \tag{18}$$

$$B_i(0) = -c_1c_5(1 - a/d - 2b/d), \tag{19}$$

$$C_r(0) = D_r(0) = [c_1c_5c_4 + (c_1c_2 - 1)c_3]/2\pi/(c_3^2 + c_4^2), \tag{20}$$

$$C_i(0) = D_i(0) = [c_1c_5c_3 + (c_1c_2 - 1)c_4]/2\pi/(c_3^2 + c_4^2), \tag{21}$$

where c_1 and c_2 are as defined in Section 1 and the new wavelength-dependent parameters are

$$c_3 = \beta z_0/\lambda/(b/d), \tag{22}$$

$$c_4 = \delta z_0/\lambda/(b/d), \tag{23}$$

$$c_5 = \sin(2\pi\delta z_o/\lambda). \tag{24}$$

$$2\pi mA_r(m) = -\sin\phi_a, \tag{8}$$

$$2\pi mA_i(m) = \cos\phi_a - 1, \tag{9}$$

$$2\pi mB_r(m) = c_1[c_2\sin\phi_a - c_5(\cos\phi_a - 1)]\cos\phi_b + c_1[c_5\sin\phi_a + c_2(\cos\phi_a + 1)]\sin\phi_b, \tag{10}$$

$$2\pi mB_i(m) = -c_1[c_5\sin\phi_a + c_2(\cos\phi_a - 1)]\cos\phi_b + c_1[c_2\sin\phi_a - c_5(\cos\phi_a + 1)]\sin\phi_b, \tag{11}$$

$$2\pi[(m - c_4)^2 + c_3^2]C_r(m) = (c_1c_2\cos\phi_b - 1 + c_1c_5\sin\phi_b)[c_3\cos\phi_a - (m - c_4)\sin\phi_a] - (c_1c_2\sin\phi_b - c_1c_5\cos\phi_b)[c_3\sin\phi_a + (m - c_4)\cos\phi_a], \tag{12}$$

$$2\pi[(m - c_4)^2 + c_3^2]C_i(m) = (c_1c_2\cos\phi_b - 1 + c_1c_5\sin\phi_b)[c_3\sin\phi_a + (m - c_4)\cos\phi_a] + (c_1c_2\sin\phi_b - c_1c_5\cos\phi_b)[c_3\cos\phi_a - (m - c_4)\sin\phi_a], \tag{13}$$

$$2\pi[(m + c_4)^2 + c_3^2]D_r(m) = -c_3(1 - c_1c_2\cos\phi_b + c_1c_5\sin\phi_b) - c_1(m + c_4)(c_2\sin\phi_b + c_5\cos\phi_b), \tag{14}$$

$$2\pi[(m + c_4)^2 + c_3^2]D_i(m) = (m + c_4)(1 - c_1c_2\cos\phi_b + c_1c_5\sin\phi_b) - c_1c_3(c_2\sin\phi_b + c_5\cos\phi_b), \tag{15}$$

The above equations simplify to those given in Section 1 for a rectangular bar when $b/d = 0$.

Figure 7 shows the result of applying this linear side-wall model to the same grating data given in Section 2. With a single set of physical parameters for the profile, a significant improvement in the fit to both measured efficiency ratios (η_2/η_1 and η_1/η_0) is evident compared with the rectangular bar results of Fig. 5.

Table 2 (discussed more fully below) lists the critical parameters of the linear fit and the resulting average absolute value of the fractional error Δ in the efficiency ratios η_1/η_0 and η_2/η_1.

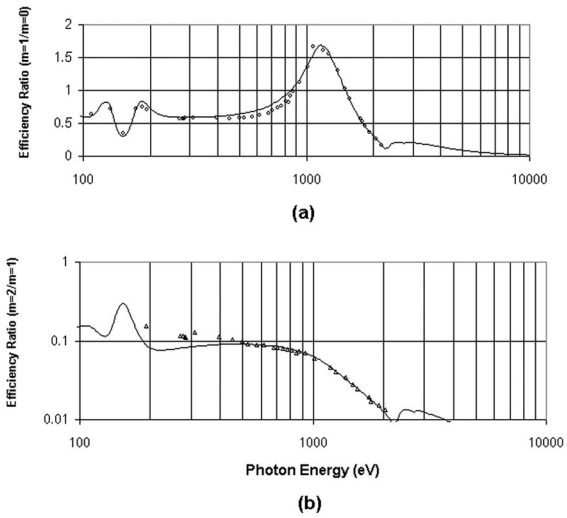

Fig. 7. HS14 efficiency ratio best fit of linear side-wall bar model ($z_o = 287$ nm, $a/d = 0.369$, $b/d = 0.114$).

B. Free-Form (Multiple Step) Symmetrical Profile Model

The next step of generalization is to consider allowing any desired symmetrical profile bar to be formed by the freedom to choose an arbitrary number of steps of individually specified heights. Referring to Fig. 8, we consider S steps of equal width Δa on each side of a plateau, and define

$$\alpha = 2\pi m \Delta a/d \tag{25}$$

$$S\alpha = 2\pi m b/d = \phi_b, \tag{26}$$

where $b = S\ \Delta a$. Our Kirchoff solution results in complex amplitude components for finite orders m as

$$2\pi m[A_r(m) + B_r(m)] = \cos\phi_a - 1 - c_1[c_5 \sin\phi_a + c_2(\cos\phi_a - 1)]\cos\phi_b + c_1[c_2 \sin\phi_a - c_5(\cos\phi_a + 1)]\sin\phi_b, \tag{27}$$

$$2\pi m[A_i(m) + B_i(m)] = \sin\phi_a - c_1[c_2 \sin\phi_a - c_5(\cos\phi_a - 1)]\cos\phi_b - c_1[c_5 \sin\phi_a + c_2(\cos\phi_a + 1)]\sin\phi_b, \tag{28}$$

$$2\pi m[C_r(m) + D_r(m)] = \sum_{j=1}^{S} E_r(m)\exp(-2\pi\beta z_j/\lambda), \tag{29}$$

$$2\pi m[C_i(m) + D_i(m)] = \sum_{j=1}^{S} E_i(m)\exp(-2\pi\beta z_j/\lambda), \tag{30}$$

where z_j is the thickness of step j and where

$$E_r(m) = \{[1 - \cos\phi_a]\cos(2\pi\delta z_j/\lambda) - \sin\phi_a \sin(2\pi\delta z_j/\lambda)\}[\cos(j-1)\alpha(1 - \cos\alpha) + \sin(j-1)\alpha \sin\alpha] + \{\sin\phi_a \cos(2\pi\delta z_j/\lambda) - [1 + \cos\phi_a]\sin(2\pi\delta z_j/\lambda)\}[\sin(j-1)\alpha(1 - \cos\alpha) - \cos(j-1)\alpha \sin\alpha], \tag{31}$$

$$E_i(m) = -\{[1 - \cos\phi_a]\sin(2\pi\delta z_j/\lambda) + \sin\phi_a \cos(2\pi\delta z_j/\lambda)\}[\cos(j-1)\alpha(1 - \cos\alpha) + \sin(j-1)\alpha \sin\alpha] - \{\sin\phi_a \sin(2\pi\delta z_j/\lambda) + [1 + \cos\phi_a]\cos(2\pi\delta z_j/\lambda)\}[\sin(j-1)\alpha(1 - \cos\alpha) - \cos(j-1)\alpha \sin\alpha], \tag{32}$$

and for order $m = 0$ is

$$A_r(0) + B_r(0) = a/d + (1 - a/d - 2b/d)c_1c_2, \tag{33}$$

$$A_i(0) + B_i(0) = (1 - a/d - 2b/d)c_1c_5, \tag{34}$$

$$C_r(0) + D_r(0) = 2(b/d)\sum_{j=1}^{S} \cos(2\pi\delta z_j/\lambda) \times \exp(-2\pi\beta z_j/\lambda), \tag{35}$$

$$C_i(0) + D_i(0) = 2(b/d)\sum_{j=1}^{S} \sin(2\pi\delta z_j/\lambda) \times \exp(-2\pi\beta z_j/\lambda). \tag{36}$$

Following an initial fit to a linear profile, we have developed a FORTRAN code STEPFIT that refines the bar

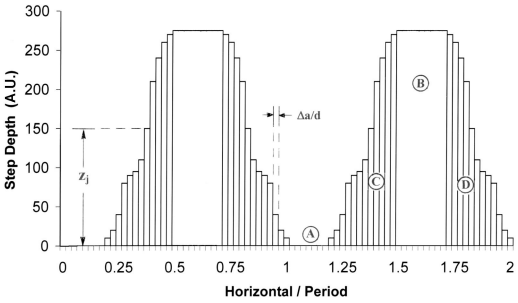

Fig. 8. Step bar thickness profile model.

shape through successive generations of numerical selection and reduced variations. This Darwinian-like computational scheme evolves the step heights defining the symmetrical profile that best fits the data in all specified spectral orders, typically $m = 1$ through $m = 4$. To provide physical robustness to the numerical results, the step heights are constrained to be monotonic on each side of the central plateau (region B of Fig. 8). As a test of the correctness of our equations and computer code, we used Eqs. (7)–(24) to generate the efficiencies for a linear profile bar. Code STEPFIT [which uses Eqs. (25)–(36)] was then run with these input efficiencies, and the output bar profile in Fig. 9 was compared to the trapezoidal profile used to generate the efficiencies. The accuracy of this simulation confirms that a trapezoid approximated by only $S = 8$ steps on each side of the plateau yields the same result as the trapezoidal model given in Subsection 3.A. This agreement between the two distinct formulations is strong indication that both are correctly derived and coded. In the final version of STEPFIT, we use $S = 29$ steps in each of the side-wall regions (C and D, Fig. 8) to obtain a high-resolution model of the bar profile.

The physical parameters of all gratings studied are summarized in Table 2. The specified line spacing (d) is confirmed with high accuracy from the measured dispersion and is also the only parameter not subject to high uncertainty during the manufacturing process. The z_o (gold-bar thickness), a/d, and b/d parameters listed are those resulting from the linear fits and are good approximations to the step-fit bar shapes given in each of the figures to be presented in Section 5. Note that the linear fits consider only ratios of the efficiencies in spectral orders 0, 1, and 2, and therefore do not consider the effect of the support structure (see Subsection 4.D). The OAR values listed result from the step fits. The linear model also does not include any organic contamination (see Subsection 4.E). The slit widths listed here were obtained by high-power optical microscopy and were confirmed in selected cases with scanning electron microscopy (SEM).

Table 2 values given in parentheses for the gold-bar thickness are those supplied by the grating manufacturer. Evident from Table 2 is both that these values are highly discrepant from the measured values and that the variation in measured thickness between gratings of the same generation is significant.

The fit errors listed in Table 2 are the sum of the errors at the individual photon energies, divided by the number of photon energies (typically 30–40).

Table 2. Parameters of Free-Standing Gratings

Grating	d (nm)	[a] z_o (nm)	a/d	b/d	[b] L-fit $\langle\|\Delta\|\rangle$	[c] Support (nm) (OAR)	[b] S-fit $\langle\|\Delta\|\rangle$	Slit (μm)
[d–f] HD6	500	108(200)	0.225	0.080	15%	2660 (0.68)	7.2%	70
[e–g] FS194_Z	200	400	0.324	0.143	9.8%	820 (0.43)	12.1%	64
[f] X27	400	317(175)	0.396	0.062	9.1%	770 (0.34)	5.5%	152
[f] X21	200	308(500)	0.262	0.089	8.2%	770 (0.30)	5.0%	151
HS04	200	206	0.354	0.133	9.8%	710 (0.76)	3.3%	70
HS06	200	276	0.370	0.122	9.6%	930 (0.71)	3.7%	70
HS14	200	284	0.376	0.108	7.7%	890 (0.71)	2.5%	70
[h] HS14_Z	200	284	0.355	0.130	10.5%	890 (0.73)	3.8%	70
HS17	200	212	0.360	0.118	6.6%	1000 (0.58)	4.6%	70
HS05	200	271	0.376	0.122	11%	890 (0.71)	4.2%	70
HS09	200	253	0.391	0.176	10.9%	890 (0.70)	4.2%	70
XS01	200	192(340)	0.355	0.131	7.9%	710 (0.79)	4.7%	70

[a] Calibrated z_o values from this study are compared with values specified by the manufacturer (in parenthesis).

[b] L-fit is the accuracy of efficiency ratios (1/0 and 2/1) with a linear (trapezoidal-like) fit (Subsection 3.A), and S-fit is accuracy of weighted absolute efficiencies (typically 1, 2, 3, 4) with a multistep (free-form) fit to the side-wall profile (Subsection 3.B).

[c] Support structure is gold for HD6 and FS194_Z and is nickel for all others. OAR is the open-area-ratio of support structure.

[d] HD6 manufactured by Heidenhain GmbH; all others manufactured by MIT Space Nanostructures Laboratory.

[e] HD6 and FS194_Z calibrated with SNR monochromator; subsequent series gratings calibrated with SXR monochromator.

[f] HD6, FS194_Z, X21, and X27 calibrated with early model Photometrics CCD; subsequent gratings calibrating with current model Princeton Instruments CCD.

[g] FS194 inferred to have an organic film (identified by the manufacturer as black wax) residue extending well in between the gold bars, acting as a base collector of source contaminants. The current calibration of FS194_Z was after its use in the Z accelerator, which may have resulted in additional deposit of organics and debris upon the wax base; combined with the subtraction of only the detector background (no off-line spectra) for this grating the accuracy of the fits is seen to be lower.

[h] HS14_Z is HS14 recalibrated after 1 yr on the Z source.

Table 3. Calibration Uncertainties

Source stability	<0.5%
Photon- or noise-counting statistics	<0.3%
Dark current stability	<0.2%
CCD spatial nonuniformity	<1%
CCD temporal nonlinearity	<0.5%
Monochromator spectral impurity	<0.2%
Illumination gradient (averaged)	<0.5%
Grating efficiency gradient (averaged)	<0.5%
Grating support ripple (averaged)	<2%
Grating scatter	1%–3%
Slit width and alignment calibration	<2%
Bar profile nonuniformities (e.g., ripple)	1%
Support structure model	1%
Organic contaminant model	1%
Total rms error at each photon energy	3%–5%
Total rms average error (36 photon energies)	0.5%–1%

These results are scaled to the first-order efficiencies. In the case of the step fits, the errors in the higher orders are therefore weighted correspondingly less owing to their lower efficiencies.

4. Practical Effects and Sources of Error

Table 3 lists the major sources of calibration error and an estimate of the magnitude of each. A discussion of practical effects contributing to these errors follows.

A. Source Stability

1. *Source Motion*

As the source is used in place of an entrance slit, changes in its position (due to differential expansion within the source during heating of the anode and its copper high-voltage probe) affect the selected photon energy and intensity passing through the fixed exit slit. At the early stages of this research, this motion was characterized by accurate (0.0005″) repositioning of the source as a function of time, line species, and source power. We obtained a factor of ~5 reduction in the source motion by upgrading the commercially available source with forced (double-fan) air cooling around an enlarged copper fin radiator in conductive contact with the anode. Allowing the source to warm up for ~1 h prior to data collection and readjusting the source position (0.0005″ precision) until the intensity changed by less than 1% between reference slit exposures before data was taken further minimized the effect. Multiple (eight) reference slit exposures are made symmetrically spaced in time around the two online and the one off-line grating exposures; therefore only a nonlinear change versus time in the transmitted source flux would result in an error to the calculated efficiency.

2. *Source Intensity Change*

By maintaining a clean source and anode surface, operating the source only at vacuum pressures less than 2×10^{-7} mbar (typically in the 10^{-8} range), and selecting the lowest power readings and exposure times needed to provide the required S/N ratio (typically >300), it was possible to minimize the accumulation rate of hydrocarbons. Typical source operating parameters were a 10-kV anode voltage and a 0.20-mA emission current. The fan cooling (mentioned in Subsection 4.A.1) also seemed to reduce the rate of hydrocarbon contamination owing to lower anode temperatures.

The combination of source motion and inherent change in source intensity produced intensity changes at the detector whose residual nonlinearity with time was measured to be less than 0.5%.

B. Monochromator Stability

1. *Spectral Impurities*

The spectral separation ($\Delta E/E$) between the off-line and the online settings [ref. Eq. (6)] was chosen individually for each spectral line, to minimize the spectral contamination while maintaining a high net signal after the subtraction. The selection of thin-film filter material and thickness (Table 1) was also made to further remove any residual higher-order or scattered radiation otherwise remaining after the off-line subtraction. Typically there were no spectral impurities detectable after this procedure (see Fig. 4), so we estimate the amount of such impurities to be less than 0.2% relative to the $m = 1$ efficiencies.

2. *Temporal Stability*

Any unintended movement of the optics or slits of the monochromator relative to each other or the source causes changes to the transmitted intensity and photon energy. Hettrick Scientific monochromators provide the critical physical and hence optical stability by use of only stationary slit designs. Therefore, for both the SNR and the SXR monochromator-based

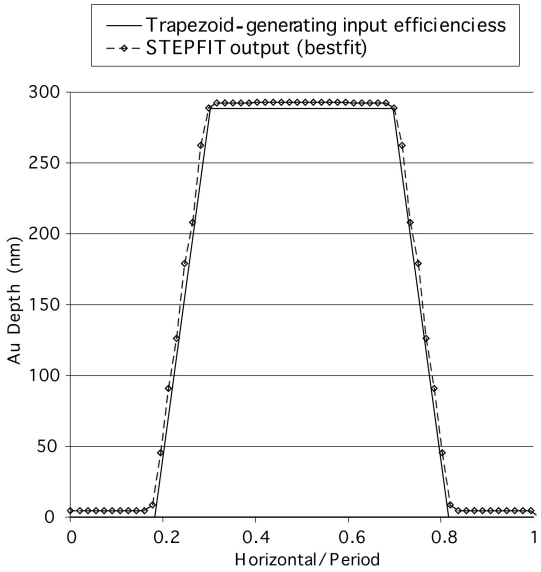

Fig. 9. STEPFIT test for a trapezoidal bar, demonstrating the correctness of the new Kirchoff solutions derived in this study for both a trapezoidal and a multistep profile bar.

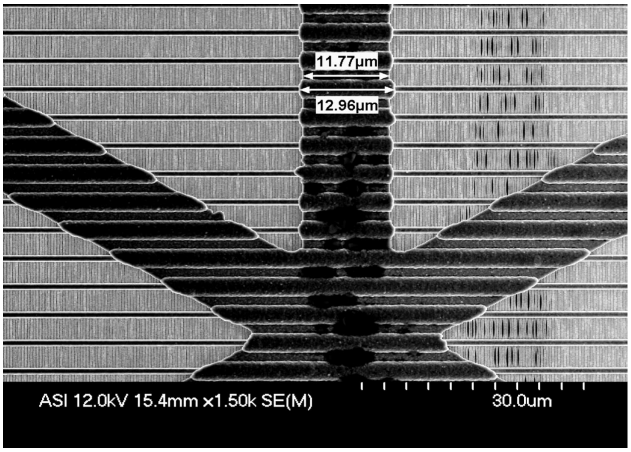

Fig. 10. SEM of grating HS04 at 1.5-k magnification, showing nickel support structure composed of a triangular coarse pattern and a linear fine pattern. Bending of gold grating bars is also evident to the right of the micrograph.

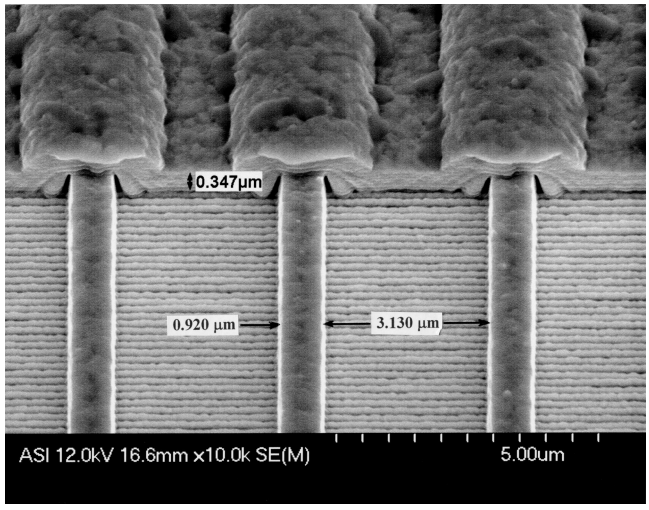

Fig. 11. SEM of grating HS04 at 10-k magnification, taken at an elevation of 45°, measuring the projected thickness of the coarse supports and the width of the fine support bars.

calibration systems, the transmitted intensities were measured to be constant with a nonlinearity of less than the 0.5% calibration error already included in Subsection 4.A.

C. Charge-Coupled Device Detector

1. Photon-Counting and Dark Current Statistics

To ensure a statistical accuracy of better than ~0.3%, we have chosen accumulated exposure times such that the number of detected photons exceeds $N_p \sim 10^5$ for the combined first orders at each photon energy. Given the work function of silicon ($W = 3.63$ eV/e^-) and the electronic gain ($G = 4.2$ e^-/ADU; ADU, analog-to-digital unit), this statistical accuracy requires a number of electronic counts equal to $(N_p/G) \times (E/W)$, which depends on the photon energy E. For example, Fig. 4 shows an integrated sum of $\sim 1.2 \times 10^6$ ADU/pixel $\times$ 10 pixels/order $= 1.2 \times 10^7$ ADUs in the combined first orders at *Y*–*M*. At $E =$ 133 eV, this sum converts to $\sim 1.4 \times 10^6$ photons, yielding a statistical error of less than 0.1%.

2. Detector Background

The two-dimensional (2-D) image of each spectral order at the CCD is typically ~10 pixels (0.2 mm) wide and ~150 pixels (3 mm) long. Given a dark current of 0.2 e^-/s/pixel, this 2-D area results in a dark current of ~300 e^-/s ~70 ADU/s. A typical exposure time per frame is 300 s, resulting in a detector background of $\sim 2 \times 10^4$ ADUs. As this exposure is small in comparison with the number of counts from incident photons (Subsection 4.C.1) in $m = 1$, its statistical effect on the net accuracy of the data can be neglected. Note that detector background can limit the statistical accuracy of the data in weak spectral orders, but the resulting weighted effect on the overall grating efficiency is correspondingly reduced.

Because our calibration provides for the subtraction of this dark current [Eq. (6)], the only significant effect on the accuracy of our results is its stability. This effect depends on the constancy of chip temperature (thermostatic precision), which was poor (±1 °C) for the Photometrics CCD and excellent (±0.05 °C) for the Princeton Instruments CCD. In the latter case, the resulting small change in dark count rate with time was effectively canceled by our procedure of taking reference slit exposures both before and after each of the grating exposures. The residual has the effect mainly of changing the level of the spectrum baseline and is estimated to contribute less than 0.2% error in the grating efficiency calibration.

3. Temporal Nonlinearity

In the Photometrics CCD, we found that the accumulated counts did not increase linearly with exposure time, even when far below the saturation limit. The Princeton Instruments CCD (PI-SX) showed this ef-

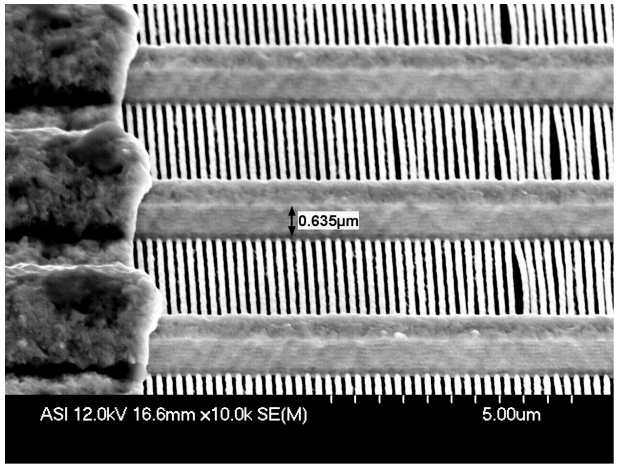

Fig. 12. SEM of grating HS04 at 10-k magnification, taken at an elevation of 45°, measuring the projected thickness of the fine nickel support bars. Extreme bending of the gold grating bars is evident.

fect to a smaller extent. We reduced the remaining temporal nonlinearity to below 0.5% by choosing a short exposure time (typically 300 s) for all frames and varying only the number of frames as required for maintaining a desired S/N ratio level. The use of identical exposure times also eliminates the systematic error that would result from the fixed finite readout time (~1 s for the PI-SX CCD) added to different intended exposure times.

4. Spatial Nonuniformity

We tested spatial nonuniformity at $E = 108.5$ eV by filtered source illumination in the absence of any optics and found it to be less than 1% over the measurement region of interest of the PI-SX CCD.

D. Transmission Grating Support Structure

1. Transmission

An electron micrograph of a grating (denoted HS04) selected for autopsy after soft-x-ray calibration is shown in Figs. 10–12. The HS-series gold grating bars are supported by two nickel structures: (i) a fine linear pattern with bars of nominal width (1 μm), gap (3 μm) [e.g., Fig. 11 shows an OAR ~3.1/4.0 = 0.78], and thickness (approx. 0.9 μm) [0.635 μm/cos(45°) from the 45° inclined perspective shown in Fig. 12], and (ii) a coarse equilateral triangular pattern structure with 400-μm on-center spacing, OAR~0.90 (Fig. 10), and thickness (approx. 0.5 μm) [0.347 μm/cos(45°) from Fig. 11]. The combined fine and coarse structures thereby have a net OAR ~$0.78 \times 0.90 = 0.70$. The fine nickel support structure of the X-series gold gratings had an unintentionally small geometric transmission, owing to wider (2.5 μm) bars and narrower (1.5 μm) gaps, resulting in a net OAR of only ~0.34.

We canceled the effect of the nickel support structures in the linear model (e.g., Fig. 7) by fitting the gold-bar parameters to ratios of measured efficiencies. However, in the STEPFIT routine, the gold-bar and nickel support structure parameters are jointly optimized by our fitting the measured absolute efficiencies. In these calculations, the support structure transmission model is ideally the product of the transmissions for the fine and the coarse structures. However, we have found that a single-component model produces fits indistinguishable from those that use two separate thicknesses and OARs. Therefore, to quicken the iterative computer calculations, we have used the following expression for the net support structure transmission,

$$T = OAR + (1 - OAR)\exp(-4\pi\beta\tau/\lambda), \quad (37)$$

where β is the imaginary component of the refractive index of nickel at wavelength λ, *OAR* is the net OAR, and τ is the effective thickness of the combined structure. The wavelength dependence of the support structure transmission decreases the transmission at the low energies and at the high-energy side of the Ni–L edge at 852 eV. Both effects, while undesired,

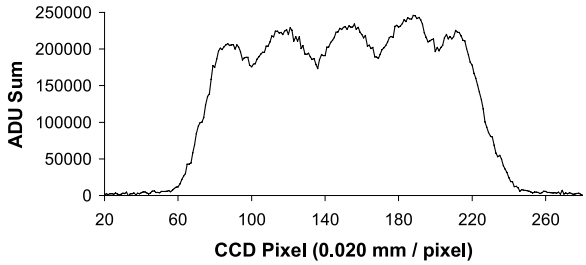

Fig. 13. Image profile in the astigmatism direction (along the length of the grating aperture slit, vertical in Fig. 10) at the CCD, taken at a photon energy of 851.5 eV.

provide excellent constraints by which to fit the two adjustable physical parameters to the soft-x-ray data. The inferred OAR and thickness parameters were in agreement with direct SEM inspection measurements (Figs. 10–12) to within ~1% in the resulting transmission.

2. Diffraction

The fine (4-μm period) linear nickel support structure is a diffraction grating in its own right, albeit at a dispersion 20 times lower than the intended (gold) grating. Given the nickel bar and space widths measured in Fig. 11 and the nearly opaque thickness of ~0.9 μm = 0.635 μm/cos(45°) measured in Fig. 12, the energy diffracted into the various spectral orders of this nickel grating can be calculated from Eq. (1)—with $a/d = 0.75$ and $c_1 = 0$—to be ~5% (each of $m = \pm 1$), 2.5% (each of $m = \pm 2$), and <1% (each of $m = \pm 3$). At the lowest photon energies in the soft x ray (100 eV), this nickel grating disperses the $m = \pm 3$ radiation at an angle of ±0.54 degrees out of the dispersion plane of the gold grating. At the CCD distance of ~200 mm, this converts to a linear displacement of ±1.8 mm. Fortunately, this radiation is included in the intensity summed over the 6-mm-long region of interest read by the CCD in this direction and therefore does not represent a significant source of error.

3. Spatial Ripple

The low-frequency ripple shown in Fig. 13 for grating HS14 is due to the triangular pattern coarse nickel support structure intercepted by the grating aperture slit whose minor width (70 μm) is in the horizontal direction of Figs. 10 and 13. This ripple is measured along the length of the slit and is present with all gratings from series X, HS, and XS; however, the period and magnitude of the ripple depends on the position of the slit relative to the nearest vertical support bar. For example, if the slit is centered over a support bar, the ripple period equals the 400-μm, on-center period of the support structure; whereas if the slit is midway between support bars, the ripple period is half this amount (with a corresponding reduction in the amplitude) because of interception of the two other legs of the triangle for every one vertical leg of travel in the vertical direction. The measured period at the CCD is the period at the grating pro-

jected geometrically from the spatial focus of the monochromator located approximately 38 cm prior to the grating, yielding a magnification of $\sim(38 + 19)/38 = 1.5$. Thus, the 650-μm period shown in Fig. 13 corresponds to ~430 μm at the grating, inferring the slit is centered over one of the support bars in the case of HS14. The magnitude of the ripple is also determined by the transmission of the nickel support structure and therefore depends on the photon energy.

Because of the finite-size *Z*-pinch source and the finite size of the diode apertures, the radiation detected at any one photon energy by the spectrograph with these gratings is averaged over ~0.3–0.5 mm of grating aperture. This width is due to the projected finite source size and diode aperture and corresponds to ~1 period of the ripple. As this largely diminishes its effect, we adopt the mean value obtained by our averaging over the several periods contained along the entire illuminated slit length during the efficiency calibration. However, there is a residual digitization error due to the finite number of periods (~1) sampled in the fielded spectrograph. For example, if the sampling is over 1.5 periods, then the error in this average can be ~±8% of the amplitude of the peak-to-valley ripple, depending on where the average is taken (i.e., over two peaks and one valley or two valleys and one peak). This introduces a maximum error of ~8% × 20% ~2% in calibrated efficiency.

E. Organic Contaminant Model

The soft-x-ray efficiency data reveal the presence of a carbon-containing (organic) contaminant between the gold bars for nearly all the gratings tested. For the FS-, X-, HS-series gratings, this contamination was first inferred by the significant decrease in first-order efficiency at low energies, particularly in the case of FS194_Z, which showed clear absorption edges from carbon and oxygen (see Fig. 27 below). In addition, however, the HS-series efficiency data showed the interesting spectral characteristic of a sudden rise in the $m = 2$ efficiency to the high-energy side of these edges (see Figs. 19, 20, and 28 below). This is in the opposite direction to what would be expected if an (absorbing) organic film was covering either the entire grating structure or the gap region between the gold bars. However, the observed inverse edges are consistent with what one should expect from a significant amount of carbon present only on the immediate side walls of the gold bars whose width is nearly equal to the gap distance, a, between the bars. To understand this, first refer back to the simple Eq. (1), which shows that the efficiency at $m = 2$ vanishes if $a/d = 0.50$ and rises quickly ($\sin^2$ dependence) as a/d departs from this value. So, given that a/d is slightly below 0.5 for the HS-series gratings (see Table 2), the $m = 2$ efficiency of these gratings should abruptly rise when the gap, a, suddenly decreases owing to carbon on the gold-bar side wall becoming opaque at the high-energy side of the C–K edge.

We included an organic contaminant in the step model by allowing for a fixed thickness of a material (e.g., containing carbon) to be placed at a step position in addition to the main material of the bar (e.g., gold). The complex refractive index of this contaminant is added to that of the main material, in proportion to thickness, as required for calculation of the net absorption and phase change after transmission through both materials. FORTRAN code STEPFIT includes the thickness of this material, the starting step position, and the number of (adjacent) steps as additional adjustable parameters for which the iterative calculations optimize the fit. During initial testing of this augmentation to the code, we manually changed the input chemical composition of the assumed organic contaminant among 30 different possibilities until the best fit was achieved. Regardless of the grating, the best fits resulted from a composition defined by the elemental abundance ratio CO_3H_{10} present on the outer edges of the sloped sides of the bar profiles. This fit results not only from the spectral discontinuities at the C and O edges but also from the characteristic effects of continuum absorption by each of the three elements (C, O, and H) on the spectral shape of the efficiency curves. The presence of both carbon and oxygen is consistent with this organic contaminant being the residue left behind during an incomplete etching of either the photoresist or the antireflection coating used during various steps of the grating fabrication. The fits infer a mass ratio between this contaminant and the gold bars of nominally 1% (with a factor 3 variation between gratings); however, even such a low concentration shows a clear effect on the efficiencies at low energies.

The presence of an organic contaminant is evident from energy-dispersive comparison spectra taken of the side walls of grating HS04, as shown in Fig. 14. While the absolute magnitudes of the concentrations shown are not relevant, the increase in the amount of carbon on the sides, compared with the tops, of the bars validates the presence there of an organic as inferred by STEPFIT.

There is also a rough correlation between the amount of CO_3H_{10} inferred to be present and the accuracy of the fit, which suggests that our simple model of the organic distribution is not exact, particularly in the fit near the absorption edge of carbon (see the discussion of Section 5, below). Given the magnitude of these minor discrepancies, we estimate the average error due our organic contaminant model is typically 1% times the calculated efficiencies.

F. Transmission Grating Scatter

Any nonperiodic components to a grating diffracts radiation between the spectral orders that express a strict periodic structure. Sources of deviation from strict periodicity are evident from even a casual view of the SEM photographs for grating HS04:

1. Nickel particulates (Figs. 14–16),

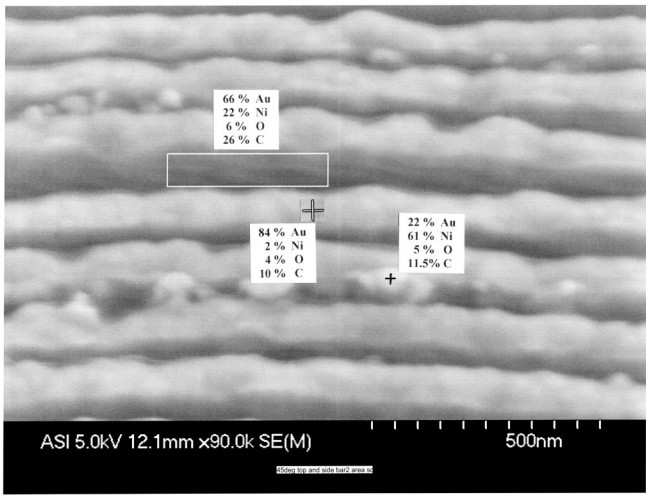

Fig. 14. SEM at 45° elevation and energy-dispersive spectral results on grating HS04: rectangle contains organic residue on side of gold bar; white cross is on top of gold bar; black cross is on nickel particulate. Listed next to each of three regions sampled by an SEM x-ray spectrometer are approximate percentages by mass of four elements along the spectrometer line-of-sight.

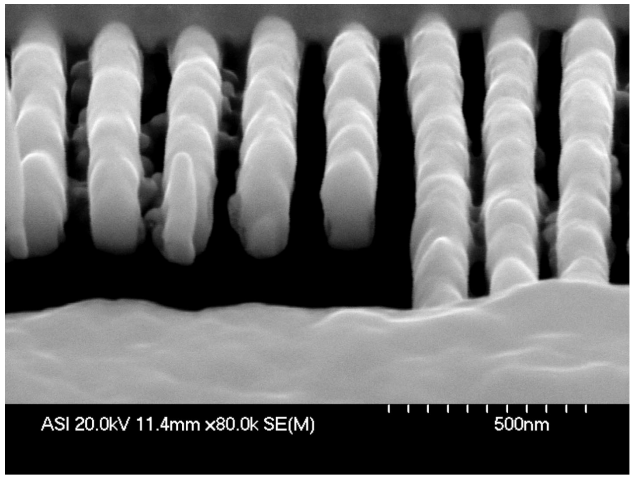

Fig. 16. SEM of sectioned gold bars of grating HS04 at 80-k magnification, taken at an elevation of 30°. The quasi-trapezoidal cross section of the bars can be seen, as well as the presence of nickel attached to the bottom edges of the gold bars. The high-frequency ripple in the gold-bar width and thickness is clearly visible.

2. Gold-bar bending and misplacements (Figs. 10 and 12),
3. High-frequency ripples (corrugations) in the gold-bar thickness and width (Figs. 14–17), with Figs. 15–17 being taken after a physical cross sectioning of the gold bars in order to view the bars in profile.

The presence of nonuniformities in such gratings has also been noted by others.[3,16,17] Note that in Fig. 15, the nickel that should appear only at the base of the fine support bar (running horizontally along the top of the figure) extends in particulate form well into the open gold grating region below it, and therefore represents contamination of the gold bars and a source of grating scatter. The extreme unevenness of the spacings shown in this figure is believed due to the physical cross sectioning of the gold bars, which took place before this SEM was taken, although spacing irregularities are also obvious in the undisturbed grating shown in Fig. 12.

Comparing Figs. 4 and 18 for gratings with different levels of resulting scatter and the corresponding fits (see Section 5, Figs. 19 and 20 below, respectively), one can see that the fit accuracy is limited largely by the scatter of the test grating, with the lower scatter grating (HS14) also showing the lower error in the model fit. Specifically, a major component of the calibration error for many of the gratings in the HS series is the inability to determine an accurate baseline [value of $GRAT_{m}$_BASE in Eq. (6)] for the

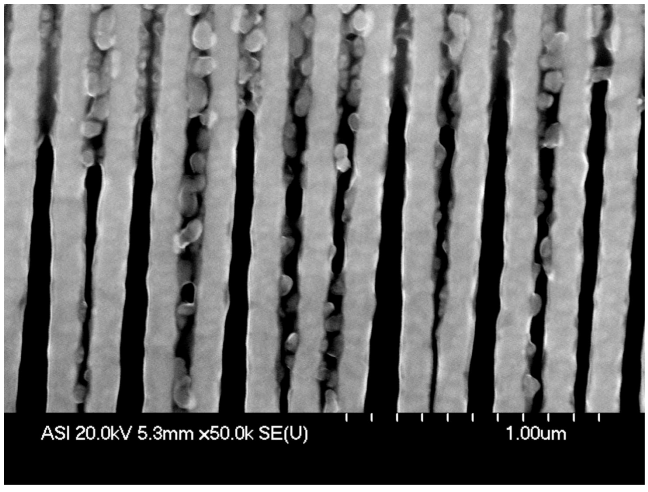

Fig. 15. SEM of grating HS04 at 50-k magnification, taken after physical sectioning of the gold grating bars. Although the uneven spacing is in part due to the stresses of the sectioning, the globular nickel contamination between the gold bars as well as the high-frequency corrugations on the edges of the bars is representative of the virgin grating.

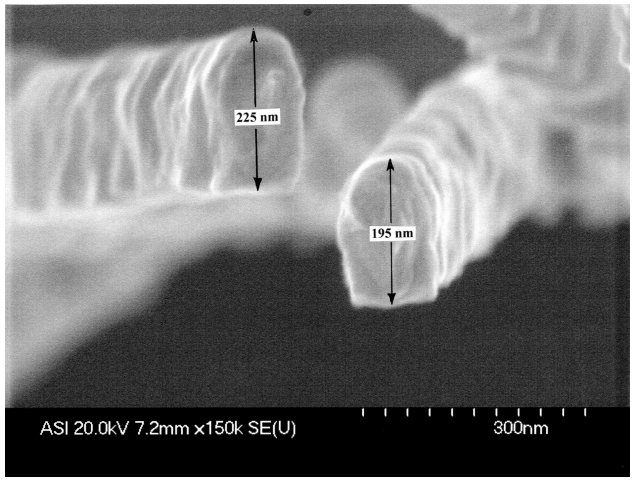

Fig. 17. SEM of sectioned gold bars of grating HS04 at 150-k magnification, viewed on-edge. The average measured thickness of ~210 nm is in excellent agreement with the thickness parameter of 206 nm inferred by the soft-x-ray efficiency data obtained with the STEPFIT code.

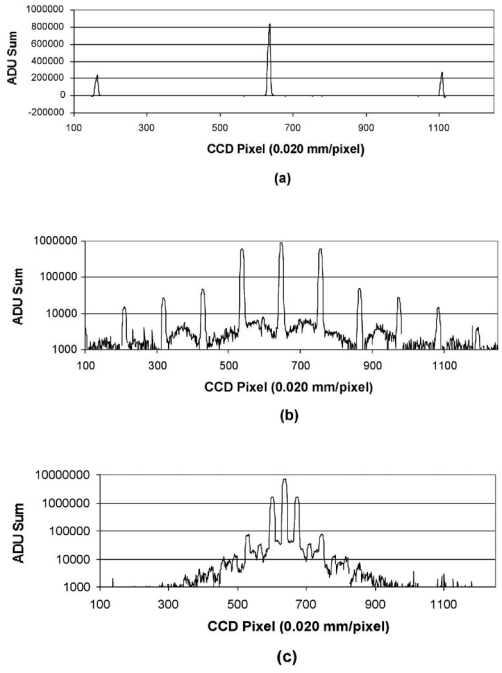

Fig. 18. HS04 order spectra at (a) Y–Mζ (133 eV), (b) Cr–Lα (573 eV), and (c) Si–Kα (1740 eV), showing high background and anomalous peaks between the spectral orders (e.g., between the fourth and the fifth orders for Si–Kα and midway between the orders for Cr–Lα). Compare with the cleaner spectra of Fig. 4 for HS14.

high scattered background lying beneath the specular orders. Judging from a comparison of similar measurements of gratings having different amounts of scatter, we estimate the calibration uncertainty due to grating scatter is ~1%–2%, depending on the grating, at each photon energy.

To the extent that scatter is present, the efficiency of a spectral order is ill-defined, as a functional definition must take into account the angular width of the detector that intercepts a fraction of the adjacent background in the fielded TGS. The presence of scatter therefore has the second deleterious effect of causing a systematic underestimate to the actual intensity recorded by a finite-size detector, as this includes a portion of the scattered light lying underneath and adjacent to the spectral orders. The use of spectral orders itself becomes questionable in the presence of anomalous peaks appearing between the order positions of a periodic grating, as is also evident from Figs. 18(b) and 18(c). As is shown in Table 4, we have selected for use only those gratings with a scattered light level below 1% of the first-order efficiencies and have thereby limited this systematic error component. Table 3 therefore lists the total estimated calibration uncertainty due to grating scatter as 1%–3%, being the sum of the two effects discussed above in this and the preceding paragraph.

G. Spatial Gradients

1. *Illumination Gradient*

The slope seen in Fig. 13 superimposed on the ripple is due mainly to the aperture variation in illuminated intensity of the test grating by a focusing grazing-incidence mirror in the high-resolution monochromator. Because the reference slit is illuminated with the same variation, the effect is largely canceled when we calculated the absolute efficiencies using Eq. (6). However, note that we average the intensity over the 2-D images prior to dividing the dispersed intensity by the reference intensity, so any nonlinearity in the gradient is not properly treated. Spatially resolved measurements on grating HS14_Z have shown that the portion of the gradient due to variations in grating efficiency, rather than in incident illumination, is less than 1% per millimeter.

2. *Efficiency Gradient*

Other transmission gratings for which data has been taken have displayed a larger variation in efficiency along the length of the slit, after the effect of the monochromator illumination has been removed. Up to ~10% gradient per millimeter was measured for one grating, and further calibration as a function of this spatial coordinate is required both for more accurate quantification of its magnitude and for determination of whether the magnitude is due to a gradient in the gold-bar a/d ratio or its thickness. As such gradients adversely affect the net calibration accuracy of the grating, we reject gratings whose gradient in $m = 1$ efficiency exceeds 1% per millimeter. In addition, to minimize the effect that this residual gradient has in the calibration of the fielded spectrograph, we center the calibration setup illumination of ~2 mm along the length of the 6.5-mm slit (series HS and XS). In this way, the average efficiency resulting from these measurements is representative of the same central portion of the grating aperture, which is projected onto the pin diode detectors to record the spectrum of the TGS. However, because of an estimated off-centering of 0.5 mm between the calibration and the spectrograph l-o-s, we estimate the effect of a 1% per millimeter gradient in grating efficiency to be a 0.5% error in the calibrated efficiency, as included in Table 3.

H. Slit Width and Alignment Calibration

Equation (6) requires accurate knowledge of the widths of the slits used to aperture the grating and as a reference to provide a measure of absolute efficiency. As these slits interchangeably also act as the exit slit of the calibration monochromator, the variation in intensity incident across the width of the slits is a function of the source spectral line profile, the source size, and the dispersion and focusing of the monochromator. The worst case is for spectral lines whose width is similar to the slit width, resulting in the maximum change in transmitted intensity as a function of a change in slit width. To avoid this problem, we have taken care to use a reference slit of the same size (± 0.5 μm) as the grating slit. The residual uncertainty in Eq. (6) can be estimated by assuming the slits are uniformly overilluminated, resulting in a fractional error in efficiency equal or less than twice the fractional error in slit width. As the

Table 4. Summary of Critical Performance Indices

Grating (period)	η_2/η_1 @525 eV	Scatter[b]	η_1 = First-Order Efficiency[a] @183 eV	η_1 = First-Order Efficiency[a] @2042 eV
[c]Low-energy gratings		@277 eV		
HD6 (d = 500 nm)	[d]0.342[e]	~0.01[e]	2.48%	1.1%
X27 (d = 400 nm)	0.072	0.003	2.77%	7.3%[e]
High-energy gratings (d = 200 nm):		@1254 eV		
First Generation				
FS194_Z	[d]0.240[e]	0.004	[f]0.44%[e]	7.8%
Second Generation				
X21	[d]0.369[e]	0.006	1.75%	4.9%[e]
Third Generation				
HS04	0.062	~0.02[e]	7.4%	5.8%[e]
HS14	0.092	0.007	6.4%	9.9%
Fourth Generation				
XS01	0.066	0.010[e]	9.6%	5.4%[e,g]

[a]Low efficiencies of X-series gratings are due to a low OAR of the nickel support structure.
[b]Scatter is measured as a fraction of the peak intensity at spectral order m = 1 and is considered marginally acceptable at a value of 0.01.
[c]Gratings HD6 and X27 were specified as thin-bar low-energy gratings and therefore the high efficiency of X27 at 2042 eV is unsatisfactory (because of the gold bars being nearly twice the specified thickness); all other gratings (d = 200 nm period) were specified to have thick bars for optimization at high energies.
[d]High contamination from second-order efficiency (η_2/η_1 ratio) for HD, FS, and X series results from gap-to-period (a/d) ratios that are significantly below the ideal value of 0.5.
[e]Absent soft-x-ray selection, no grating series generally conforms to the design parameters or performs acceptably in all of the three basic categories, with the *e* identifying unsatisfactory or marginal values for the intended application; selection of acceptable gratings (e.g., HS14 and a handful of others) therefore relies on soft-x-ray calibration of numerous gratings whose parameters are otherwise not well characterized.
[f]Low efficiency at 183 eV (below the carbon photoabsorption edge, see Fig. 27) for FS-series grating indicates the presence of black wax film residue from the grating fabrication process and subsequent accumulation of contaminants onto this wax film.
[g]Low efficiency at 2042 eV for XS series is due to thin gold bars (<200 nm).

accuracy in the slit-width calibration (through visible and SEM inspection) is ±0.5 μm (0.7% times the slit width of 70 μm), the maximum resulting error in efficiency calibration is 1.4%.

Because of the finite slit width, positional and angular coalignment of the reference and grating slits can also affect the absolute calibration. Each calibration system was outfitted with an *in situ* microscope, and the selected slit bright edge illuminated at high magnification both at atmosphere and under vacuum was viewed. With a cross-hair reticle, we manually performed the angular coalignment at atmosphere (to within ~2 μm over a 1 mm field of view) and confirmed it under vacuum. We performed the positional coalignment under vacuum using a feedthrough micrometer having 1-μm precision that translated the spring-loaded crossed-roller stage to which both slits were rigidly mounted. If the misalignment between the slits was 2 μm, then in the worst case of a monochromatic spectral line width equal to the slit width of 70 μm, the error in transmitted flux could be as large as 1/70, which is equal to an additional 2.8%.

However, in an initial test in which two slits of width calibrated to within ~0.5 μm were alternately selected into the beam, a change of less than 0.5% in transmitted flux was measured. This is significantly better than the sum of the worst cases of the above two sources of error, which, for the purposes of Table 2, we have estimated to be 2%.

5. Absolute Model Fits

Figures 19–23 show the results of our step model applied to the data obtained from five virgin (otherwise unused) gratings. For each spectral order, the legend lists the average relative deviation of the fit from the data. These percentage errors were weighted by the order efficiency and summed to calculate the net error for the multiple-order fit, listed in each figure caption as a percentage of the m = 1 efficiency. Note that these fit errors are added as absolute values but are for the most part randomly distributed both above and below the data. Therefore, for purposes of estimating the error in the net efficiency as integrated over all the (N ~30–40) measured photon energies, the multiple-order error should be divided by $\sim N^{1/2}$. Thus, the net error for our radiometric calibration purposes with grating HS14 would be ~2.5%/6 = 0.5%. The calibration fits for gratings X21, X27, and HD6 are somewhat worse (though still <1%), because of being done in the early stages of this research with a lower-resolution monochromator or higher-noise CCD as discussed in Section 2. The highly accurate fits provided by our new step model represent a dramatic improvement

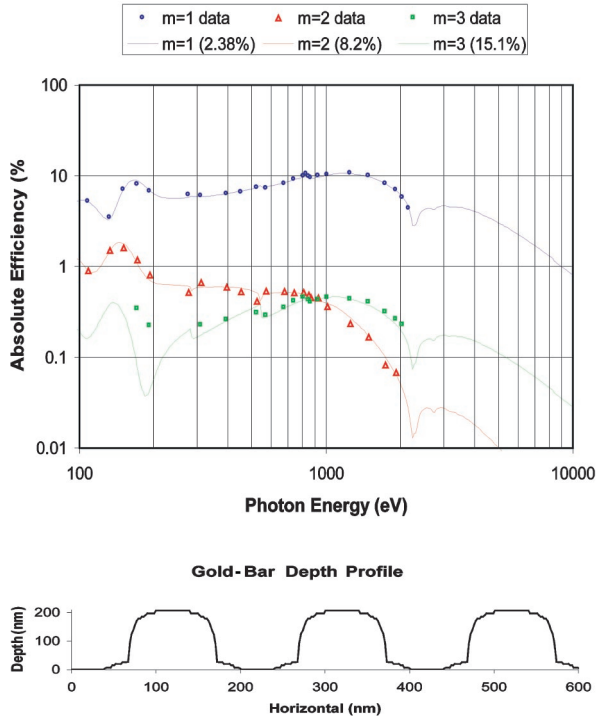

Fig. 19. Step fit for grating HS04, resulting in a net error of 3.3% times $m = 1$ efficiencies. Gold bar depth profile shown in bottom part of figure.

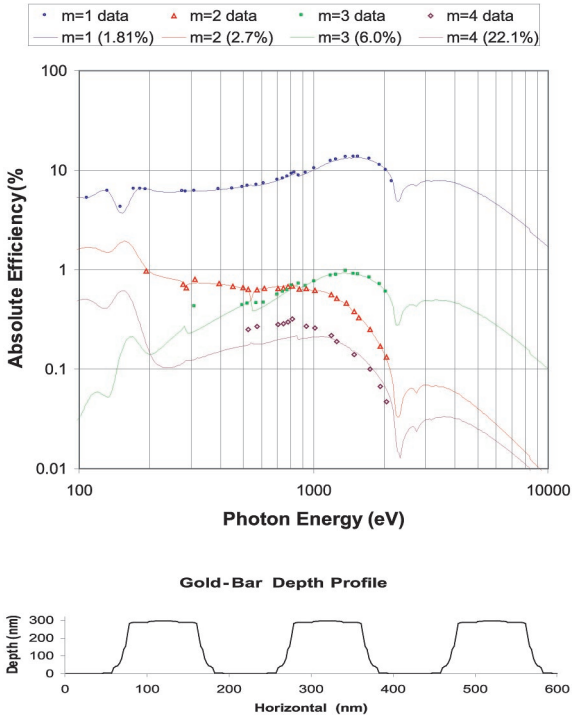

Fig. 20. Step fit for grating HS14, resulting in a net error of 2.5% times $m = 1$ efficiencies. Gold bar depth profile shown in bottom part of figure.

over those attainable with the standard (rectangular bar) model.

Table 2 includes the OAR inferred from the step-fit model calculations, as well as the average (absolute value) error of the fit as a percentage of the first-order efficiency. Because of the narrow slit width (70 μm), the OAR measured for grating series HS and XS is not simply the average OAR of the structure. It can vary by as much as 10% absolute, depending on the exact position of the slit relative to the nearest nickel bar (lying in the vertical direction of Fig. 10) of the triangular support structure. For example, if the slit is centered over such a bar, the blockage (1-OAR) due to this triangular structure is simply 12 μm/70 μm = 17%, whereas if the slit lies midway between two such bars, the obscuration is only 12 μm/(400 μm/2) = 6%.

In the case of the HS-series gratings, the model fit shows a less dramatic rise at the inverse edge of C–K than suggested by the single data point (Ag–M at 312 eV) to the high-energy side of this edge. Having retaken this data point carefully and multiple times under various conditions of the source, monochromator, and filter(s), we believe the inverted edge is accurately measured. Perhaps the actual chemical composition of the organic film is different from the 1:3:10 abundance ratio of CO_3H_{10}, which we found provides a good fit to the overall efficiency curves over the soft-x-ray energy range. Also note that an accurate modeling of this effect must depart from our simple model of an organic of constant thickness and width on each side of a uniform profile gold bar. First, as shown in Figs. 16 and 17, the gold bars exhibit significant (20%) changes in width (and depth) over 100-nm spatial wavelengths along the bar lengths. Top views of the grating bars at high SEM magnification (e.g., Fig. 15) also show suggestions of this high-frequency ripple along the bar lengths, albeit at lower contrast. Such ripple changes the magnitude of the inverse-edge effect, whose sensitivity nonlinearly depends on the deviation from the condition producing no second-order diffraction ($a/d = 0.50$). Second, nonuniformities in the actual distribution of the organic also affects the magnitude and direction of the spectral edge in the efficiency curve. This latter point can be easily appreciated from the fact that a completely uniform thin film of carbon, for example, would act as a thin-film filter in series with the grating and hence simply produce the same absorption curve (with the usual photoabsorption edges) overlaying the grating efficiency curves in each spectral order. At the other extreme, the same amount of carbon could be distributed not only just on the bar side walls, but also only to fill in the rippled recesses seen for the widths of the gold bars. In this case, the absorbing effect of the carbon would be enhanced, because of the exponential dependence of absorption with l-o-s mass, and the spectral edge would tend to more closely match the inverted spectral feature seen from the data, owing to

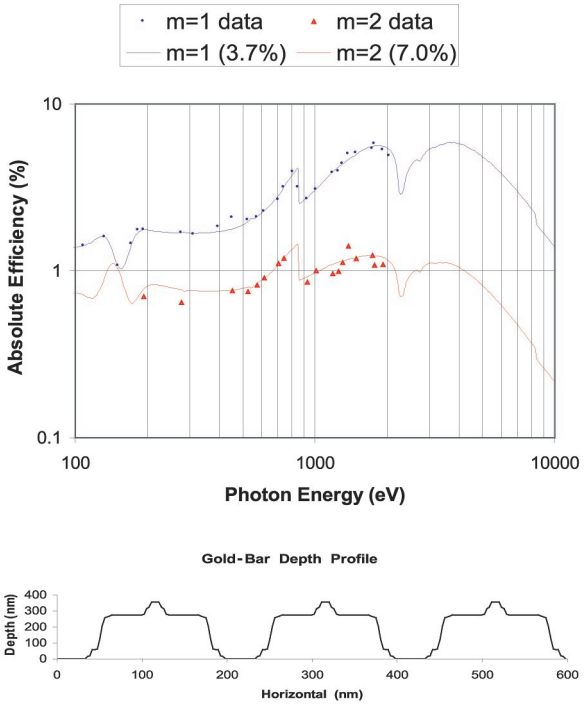

Fig. 21. Step fit for grating X21, resulting in a net error of 5.0% times $m = 1$ efficiencies. Gold bar depth profile shown in bottom part of figure.

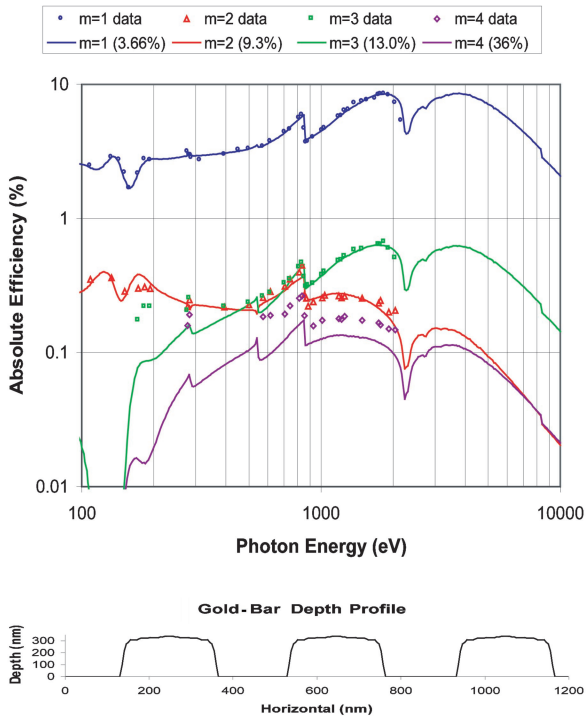

Fig. 22. Step fit for grating X27, resulting in a net error of 5.5% times $m = 1$ efficiencies. Gold bar depth profile shown in bottom part of figure.

the carbon decreasing the gap width, a, at values of a/d that are closer to 0.50 on the inside edges of the rippled width. However, such detailed modeling of this effect is not addressed here, as the present application of the grating calibration is for high accuracy in the efficiency integrated over a continuum source rather than as a function of energy over any narrow feature near these edges.

The shoulders appearing on the inferred gold-bar profiles for HS04 (Fig. 19) suggest contamination by a metallic material (having a correspondingly high absorption across the soft-x-ray energy range). Inspection of the SEMs taken for this grating, particularly Figs. 14–16, is consistent with this material being nickel. The electron microscope image of Fig. 17 displays a direct measurement of 210 nm for the gold-bar height of grating HS04. This measurement is in excellent agreement with the 206-nm value inferred from the model fit to the measured soft-x-ray efficiencies (Fig. 19), indicating that the optical constants used in our calculations are accurately representative of the gold-bar material. More general confirmation of the accuracy of the inferred grating parameters is obtained by extrapolation of the model fit from one energy region to another and by comparison of the predicted efficiencies in several spectral orders to measurements not used to constrain the fit. For example, Fig. 24 shows the efficiency curves that our model fit to measured efficiencies of grating HS18 at only three photon energies (108.5, 277, and 1254 eV). The first-order curve predicted by our physical model is extrapolated to higher energies and agrees to within ~3% times the first-order efficiencies measured in the high-energy region of 1487–5415 eV. These high-energy measurements were made with a simple transmission grating monochromator (TGM) constructed from a 1° graze angle focusing mirror and the lowest scatter transmission grating of 0.2-μm period (HS09) selected from our calibration. The scattered light of Bremsstrahlung continuum with this TGM still significantly exceeded that from our grazing-incidence reflection grating monochromators. Furthermore, this scattered light could not be accurately subtracted owing to the comparatively low dispersion (and hence off-line spectral resolution) of the transmission grating, which limited its use to only the strong characteristic lines, including the K-shell lines from 0.1 to 5.5 keV and the strong L-shell lines in the 1.9–3.4-keV region listed in Table 1.

Figure 25 is an SEM of one grating (XS01) from the most recent generation procured at the time of this writing. The reduced presence of apparent metal contaminant particles is an improvement resulting in part from information provided to the grating manufacturer on our results of soft-x-ray testing of the HS-series gratings. Table 4 shows that the level of scattered light is less than the worst case (HS04) of the HS series but is still only marginally acceptable. The source of the scatter may be the aperiodicity seen in Fig. 25 as a variable bar-to-gap ratio. The bent bars causing this aperiodicity and resulting interorder scattered light may be explained by internal

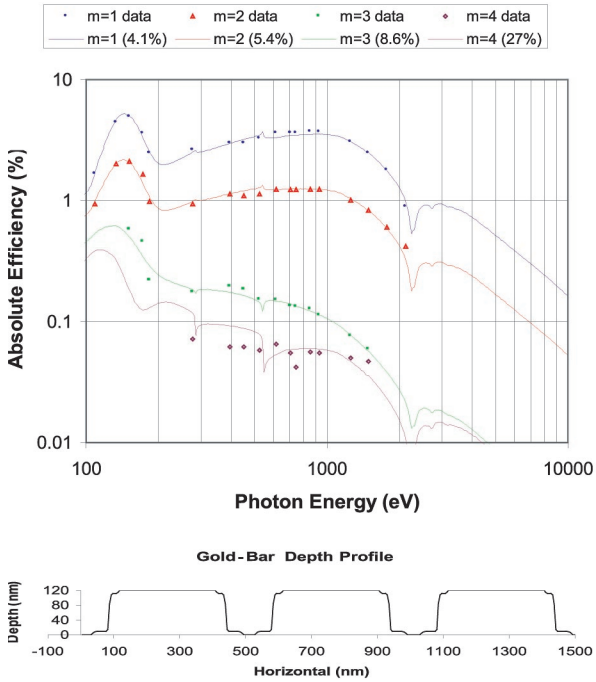

Fig. 23. Step fit for grating HD6, resulting in a net error of 7.2% times $m = 1$ efficiencies. Gold bar depth profile shown in bottom part of figure.

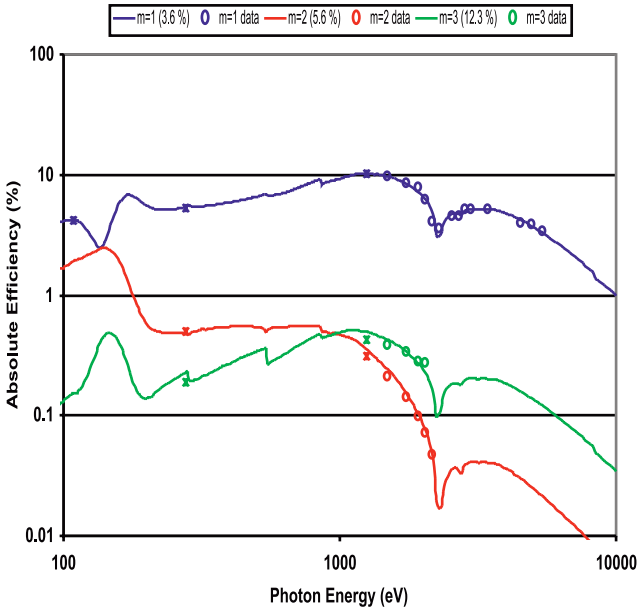

Fig. 24. Step fit for grating HS18. Model is fit to the three lowest photon energies (108.5, 277, and 1254 eV) shown by asterisks and compared with measurements (circles) made at high photon energies (1487, 1740, 1923, 2042, 2166, 2293, 2559, 2697, 2839, 2984, 3444, 4511, 4952, and 5415 eV) with a low-resolution transmission grating monochromator.

stress of the grating support structure[17] as this grating micrograph was taken by the manufacturer prior to delivery and mounting in our apparatus. Figure 26 also indicates that XS01 exhibits comparatively poor efficiency at high energies. The model fit to this data infers a gold-bar thickness that is only ~192 nm, significantly less than the manufacturer's specification of 340 nm. Similarly, a thickness ~190 nm is obtained for a second grating (XS06) in this series.

Simultaneously meeting the three performance fundamentals (efficiency, scatter, and high-order contamination) is apparently a practical problem that persists in general through the four generations of free-standing fine-period (200 nm) transmission gratings we have tested. For reference, Fig. 27 shows our first 200-nm grating calibration (FS194_Z), in which the extreme amount of a carbon-based film evident from the photoabsorption edges unfortunately precluded its continued use in the spectrographs, though its thick gold bars provided excellent efficiency at the highest energies (even greater than 2 keV). We have therefore relied on soft-x-ray calibration to characterize and select gratings of relatively high performance from among each series of gratings having the same specified manufacturing parameters.

Another difficulty of current concern is the efficiency changes we have measured following some time period after an initial calibration. For example, Fig. 28 shows the calibration of HS14 made after this grating had been used in a TGS on the Z source for ~1 yr. The significantly higher efficiencies (factor 1.3) found in $m = 2$ required that the model fit an effectively wider gold bar, as shown in Fig. 29. Changes to the second-order efficiency are the most sensitive indicators of changes in the grating bar effective width, as a result of this efficiency vanishing at $a/d = ½$. In the case of HS14, a 10-nm widening of the bars results in a factor 1.3 increase in the $m = 2$. As a second example, increases of a lesser extent (factor 1.15) to the second-order efficiency have also been measured for a grating (HS09) that was

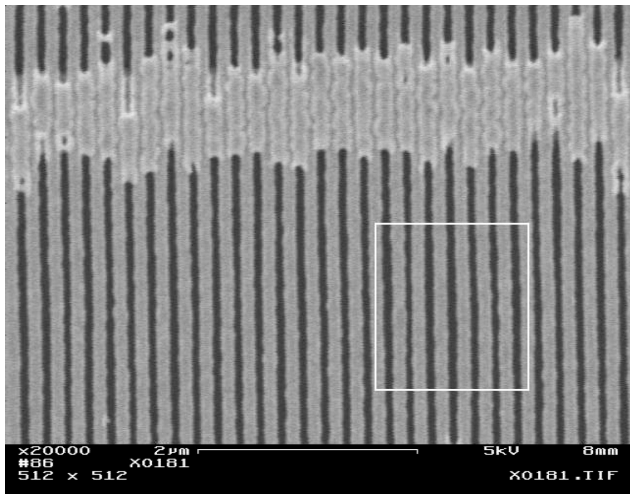

Fig. 25. SEM of last generation (XS01) grating, having fewer particulate contaminants, after feedback from this study. Significant aperiodicity is evident in the highlighted rectangle as a variable bar-to-gap ratio due to bent bars.

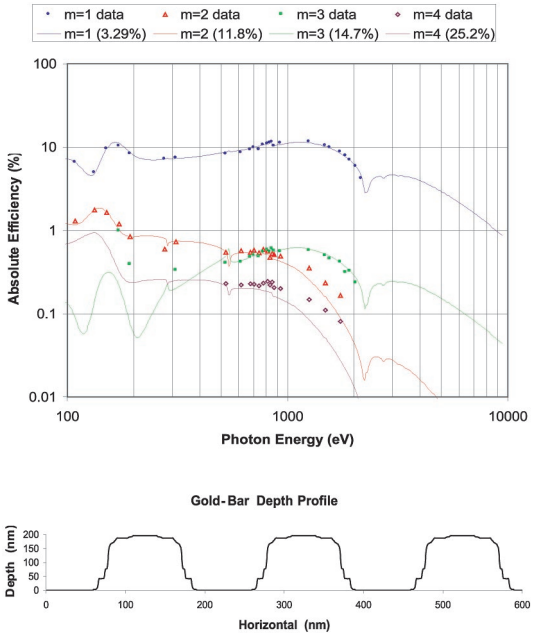

Fig. 26. Step fit for XS01, showing a thin bar and the resulting low efficiency at high photon energies. Net error is 4.7% times $m = 1$ efficiencies. Gold bar depth profile shown in bottom part of figure.

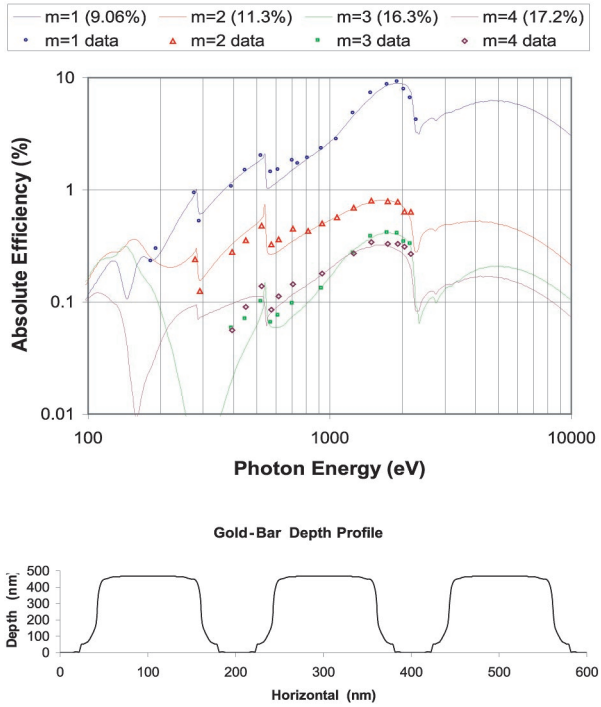

Fig. 27. Step fit for grating FS194 calibrated after use on *Z*. Net error is 12.1% times $m = 1$ efficiencies. FS194 shows a thick gold bar, resulting in excellent high energy efficiency but severe organic contamination due to black wax processing residue. Gold bar depth profile shown in bottom part of figure.

never exposed to our high-power source. It is therefore at present unclear if such changes are due to source exposure (e.g., contamination or heat loading distortions) or perhaps to a spontaneous change in the grating itself from either (i) oxidation of the organic film that apparently resides on the gold-bar side walls (even though the gratings were stored in a low-humidity environment) or (ii) stress relaxation of the support structure, resulting in a/d distortions such as observed in Figs. 10, 12, and 25. In any event, such periodic monitoring is clearly necessary to maintain accurate absolute efficiency calibration of these diffraction gratings. A third grating (HS17), which like HS09 was also not exposed to any high-power source, was remeasured 9 months after the initial calibration and did not show any significant changes in efficiency at three spot-checked photon energies.

6. *Z*-Source Diagnostic Spectra

The purpose of our extensive calibration of gratings, as reported in the preceding sections, was to provide absolute (radiometric) diagnostic information on the spectral power of tungsten wire-array *Z*-pinch soft-x-ray sources at Sandia National Laboratories.[18] In addition to the grating calibration, this process required the construction of several time-resolved TGS instruments with the gratings selected in this study. Earlier research leading to the current stage of development of these instruments and experiments has been previously reported.[3,19,20] In this section, we discuss some additional details regarding the TGS detector calibration and the unfolding of the data measured by these instruments, and we present the power spectra and time histories for two recent experiments conducted at *Z*.

A. Diode Sensitivity

To provide sufficient quantum efficiency to allow electronic detection of the soft-x-ray spectra over the subnanosecond time intervals desired, we employed high-speed silicon photodiode model AXUV-HS1, manufactured by International Radiation Detectors, Inc.[21] The small active area (0.22 mm × 0.22 mm) of these devices provides the low capacitance (100 pF) required for obtaining the fast response (0.25 ns) desired to monitor changes in the incident pulsed radiation from the *Z*-pinch source. An in-depth study of these fast diodes is given in Seely *et al.*[22] A small aperture was placed above the active area of each of 16 diodes in a linear array, allowing the continuum spectrum to be sampled across the soft-x-ray energy range.

To provide a radiometric calibration of the TGS, the measured diode voltages must be converted to irradiated power density (watts per square centimeter) at the diode apertures; hence the product of sensitivity (amps per watt) and apertured area of each diode must be known. This product is given by

$$S_j(E) = (\Phi_j/\Phi_o)\exp(-4\pi\beta_{SiO_2}\tau_{SiO_2}/\lambda)[1 - \exp(-4\pi\beta_{Si}\tau_{Si}/\lambda)]/W, \quad (38)$$

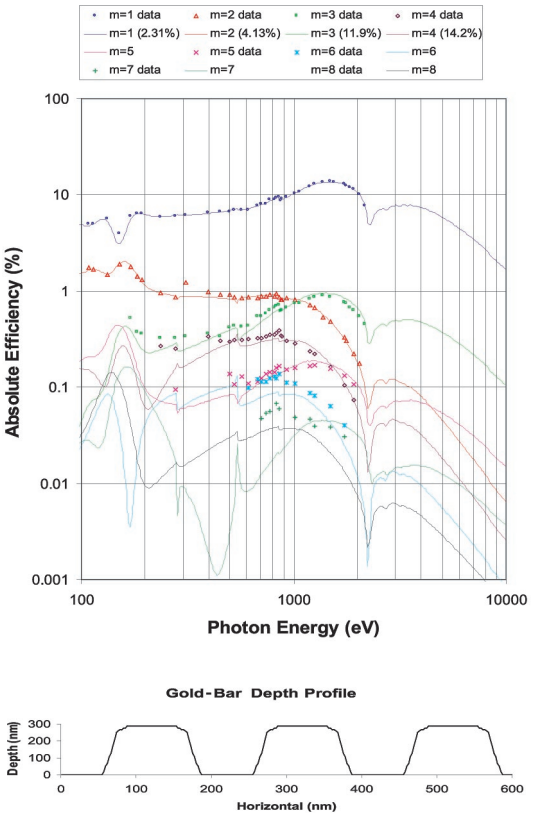

Fig. 28. Step fit for grating HS14 calibrated after use on Z, showing a slightly widened bar resulting in ~30% higher second-order efficiencies than the pre-Z results (Fig. 20). Net error is 3.8% times $m = 1$ efficiencies. Gold bar depth profile shown in bottom part of figure.

where W is the work function of silicon (3.63 eV/electron), β is the imaginary (absorption) term of the complex refractive index at wavelength λ, and τ is the layer thickness. The factor Φ_j/Φ_o is the aperture of the jth diode compared with a nominal value $\Phi_o = 5.2 \times 10^{-4}$ cm^2 and was measured by flat-fielding the 16 diodes in a uniform monochromatic beam (E ~1400 eV). The first exponential accounts for the transmission through a (preferably thin) surface layer of silicon dioxide, which is assumed to be a dead layer having no quantum efficiency. The value of τ_{SiO_2} was set to 10 nm, on the basis of upper limits set by the manufacturer and by our measurement at Be–K ($E = 108.5$ eV) of the relative response of sample TGS diodes to that of those having a known thicker (~50 nm) layer of silicon dioxide. The last factor is the desired absorption within the active silicon (a depletion layer of 100% internal quantum efficiency). The value of τ_{Si} was set to 15 μm, as roughly estimated by the manufacturer.[21] While the current results are not sensitive to this value, its more rigorous calibration will be necessary in the future when our plasma output becomes more significant in the low-absorption regions above the Si–K edge. The result is a typical value of S_j ~0.25 but is substantially lower above E ~2 keV and near the low-energy side of the Si–K edge (1740 eV) because of diminished silicon absorption in these spectral regions. The diode sensitivity is also degraded at photon energies below the O–K edge (525 eV), owing to absorption in the surface layer of SiO_2. However, with values of β tabulated for amorphous SiO_2 (glass), the sensitivity loss is only 1.2% at the lowest energy ($E = 125$ eV) sampled in any of the current TGS instruments. This loss would double (to 2.5%) if the oxide layer were actually twice as large as assumed, representing a net error of 1.3% in the lowest energy diode calibration. We adopt a conservative estimate of $\pm 5\%$ for the calibration error due to the diode's assumed physical parameters and $\pm 10\%$ for the aperture factor, at any one diode. However, note that possible detrimental effects as radiation damage and nonunit quantum efficiency within the depletion layer[22] have not been measured. Nonetheless, agreement of our spectroscopic data with total energy measurements from an independent bolometer instrument (see Subsection 6.C.1) suggests that our systematic calibration errors have not been underestimated.

B. Data Reduction

An outline of the procedures used to convert the raw TGS data to diagnosed parameters of the source is as follows:

Step 1. Use the calibration fits for the gratings to calculate spectrally continuous efficiency curves (e.g., Figures 22 and 28), by use of the new Kirchoff equations presented in Subsection 3.B. This calculation allows the grating efficiency to be known at all combinations of photon energy and spectral order dispersed to a diode position in the detection array.

Step 2. Remove (unfold) the instrumental sensitivity from the measured diode voltages. A complication is that measuring the intensity by any one diode yields the sum of all spectral-order efficiencies η_m from the grating multiplied by the source intensity at the corresponding photon energies (where E/m = constant). To perform such an unfold requires a knowledge of intensity at the higher orders before the spectrum is completely unfolded.

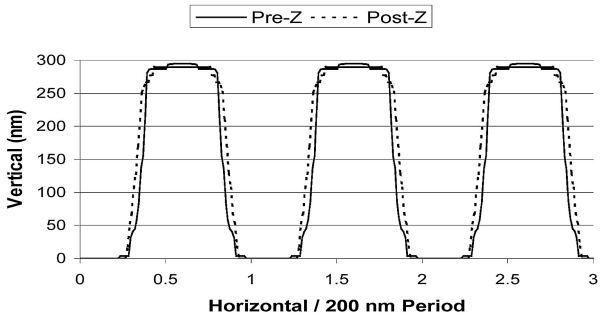

Fig. 29. Pre- and post-Z profile comparison for HS14. The post-Z bars (dotted curve) are wider by ~10 nm than the virgin bars (solid curve). It is unknown if this effective bar broadening is due to the environmental effect of the pulsed Z source and whether the gold bar actually deformed or was contaminated by the accumulation of metal debris.

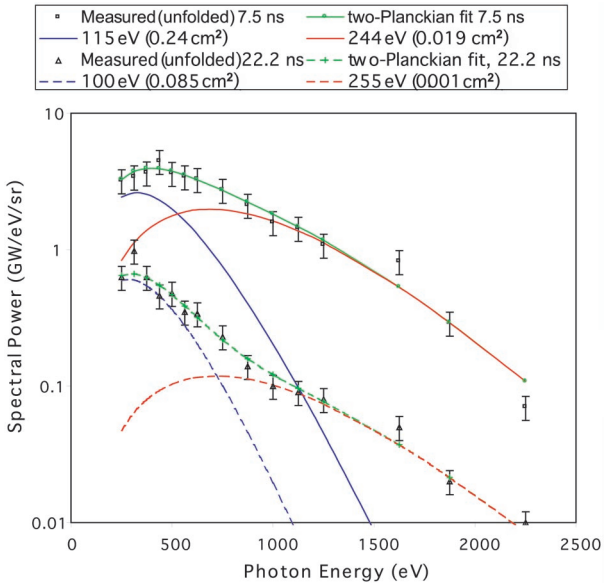

Fig. 30. Unfolded (gigawatt per electron volt per steradian) spectra of a *Z*-pinch source from experiment Z987, with grating HS14_Z on TGS5, viewing 0.40 height of the pinch at an angle of 13.5°. Data error bars are ±20%. To obtain power observable at a viewing angle of 0°, multiply the vertical scale by a factor of $1/\cos(13.5°) = 1.03$, since the high mass tungsten *Z*-pinch source is assumed to be Lambertian (optically thick). For the power spectrum observable from the full height of the pinch, divide the vertical scale by $f \sim 0.40$.

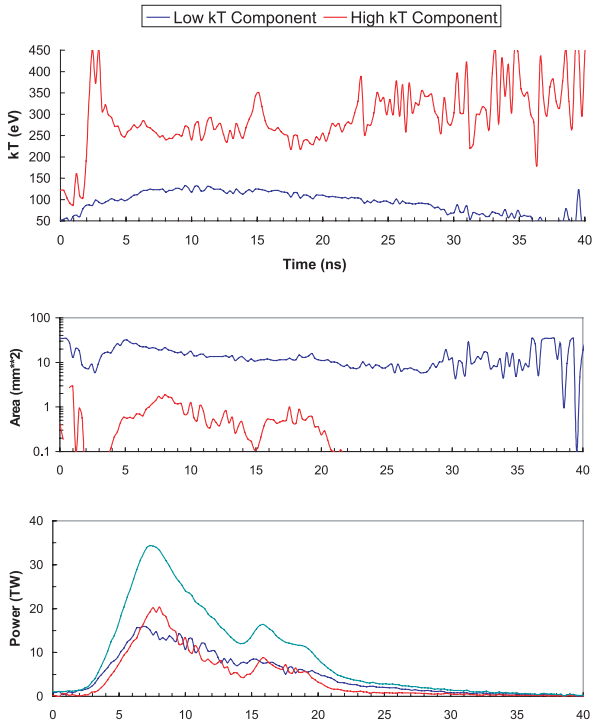

Fig. 31. Temporal history of the viewed pinch on experiment Z987. Multiply vertical scale of the power history by a factor of $1/\cos(13.5°)$ for a Lambertian emitter and by $4/\pi$ for an isotropic emitter. Energy radiated from viewed height of the pinch is thus 366 kJ for a Lambertian emitter. For the full pinch, divide this radiated energy and the vertical scale of the power history by $f \sim 0.40$. The horizontal time scale is relative.

This issue is resolved with a recursion method,[23] starting at the highest (cutoff) energies where both the incident intensities and the efficiencies at spectral orders higher than $m = 1$ are negligible. The diode sensitivity (also a function of photon energy), the geometric collection angle of the spectrograph, and the grating plate scale (dependent on the spectral order) are also included in this deconvolution. The result is a point-by-point power spectrum (gigawatt per electron volt per steradian versus photon energy) for the viewed portion of the source.

Step 3. Fit the power spectrum to a two-component Planckian,[19] by selecting the four adjustable parameters of source areas and temperatures. Alternatively, the recursive unfolding outlined in step 2 above can be avoided if the incident beam is constrained *ab initio* to be a (two-component) Planckian. In this case, the predicted voltage is calculated for each diode as the sum of the grating spectral orders convolved by the source intensities and detector efficiencies at the respective photon energies, and these are best fit to the measured voltages by choice of the Planckian temperatures and areas. This latter technique is nonrecursive and does not require the assumption of negligible higher-order grating throughput at the highest photon energies. In the case of the direct *Z* pinch (Subsection 6.C.1), it infers a total radiated energy approximately 7% lower than that inferred by the point-by-point unfolding method. This difference is due largely to the alternative weighting intervals (wavelength versus photon energy) of the resulting Planck functions and suggests that the unfolding accuracy is high. It should be understood that this is for a continuum source, and hence the unfolding is not sensitive to the limited spectral resolution imposed by the slit and detector pixel sizes as in the more challenging case of unfolding line spectra.[23] In our case, the diode detectors need only sample the continuum at a discrete number of photon energies, rather than monitor rapid changes in intensity continuously with the photon energy as would be required for optimally unfolding line intensities.

Step 4. Convert the l-o-s pinch power to power from the viewed portion of the pinch integrated over all solid angles, which depends on the optical depth of the plasma. The extreme case of an optically thin plasma is treated with isotropic emission and that of an optically thick plasma by Lambertian emission (cosine dependence on the l-o-s angle to the source surface normal). In general,

$$P = \Omega_{\text{eff}}\text{Area}(\sigma/\pi)T^4, \tag{39}$$

where σ is the Stefan–Boltzmann constant, Area and T are the source area(s) and temperature(s) inferred from the above Planckian fit, and Ω_{eff} is the effective solid angle of emission relative to intensity measured

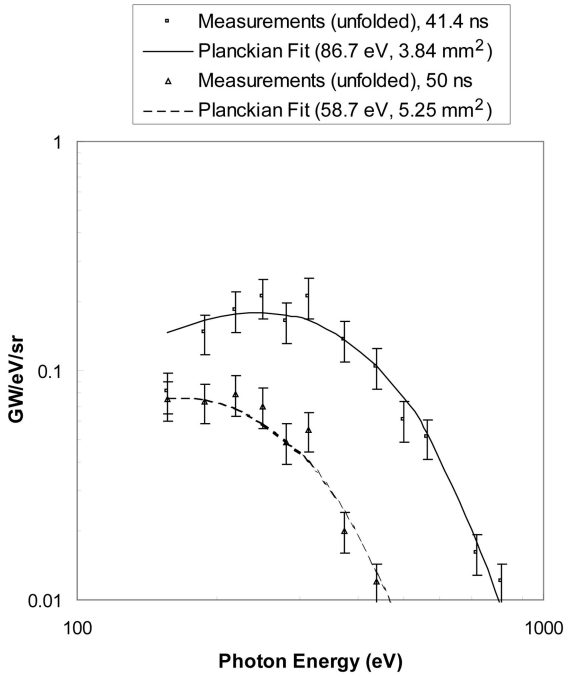

Fig. 32. Unfolded power spectrum of a gold-wall hohlraum driven by a Z pinch on experiment Z998, with grating X27 on TGS17, viewing the wall at an azimuthal angle of 29° and a polar angle of 12°. Data error bars are ±20%. Multiply vertical scale by $1/\cos(29°)/\cos(12°) = 1.17$, since the hohlraum wall is Lambertian (optically thick).

along the surface normal. In convenient units, $\sigma/\pi = 5.669/\pi \times 10^{-26}$ TW/mm^2/°K^4/sr. In the case of Lambertian emission,

$$\Omega_{\text{eff}} = \pi^2/\cos\,\rho,$$

if the spectrometer views a cylindrical source, (40)

or

$$\Omega_{\text{eff}} = \pi/\cos\,\rho/\cos\,\theta,$$

if the spectrometer views a plane source, (41)

where the cylindrical source has a vertical axis of symmetry, ρ is the l-o-s angle inclined above the horizontal plane, and θ is the l-o-s angle relative to the surface normal in the horizontal plane. In the case of isotropic emission,

$$\Omega_{\text{eff}} = 4\pi,$$

if the spectrometer views a cylindrical source, (42)

or

$$\Omega_{\text{eff}} = 2\pi,$$

if the spectrometer views a plane source. (43)

The factor Ω_{eff} accounts both for the effective area inferred from the spectrometer l-o-s viewing direction relative to the surface and for integration over the hemisphere of outward-going emission at each point on the surface of the source. These equations calculate the power radiated from both the front and the back sides of the cylinder, or from the front side of the plane source. Note that T(°K) = kT(eV)/k, where $k = 8.62 \times 10^{-5}$ eV/°K is the Boltzmann constant; therefore a plasma with $kT = 86$ eV has a temperature of 1 million Kelvins.

Step 5. Integrate the power over time for it to be converted to radiated energy and divided by the fraction (f) of the source in view to obtain the energy radiated by the full source.

C. Transmission Grating Spectrometer Results

With the accurate grating calibrations presented in this research and the diode sensitivity calculations and data-reduction technique outline above, scientific results from two Z spectrographs are reported here.

1. *High-Energy TGS5*

This spectrograph employs grating HS14 (by use of the HS14_Z calibration results of Fig. 28) and is used as a high-energy diagnostic directly viewing the Z pinch. The pinch–grating distance is 24.272 m, and the grating–detector distance is 0.603 m. The l-o-s of TGS5 views a cylindrical pinch (vertical axis of symmetry) at an angle of $\rho = 13.5°$ relative to the horizontal, and we assume f ~0.40 based on independent diagnostics. Reduced results of one such measurement are shown in Figs. 30 and 31. The error bars for individual data points are set to ±20%, which was derived as a worst-case result from the following components: (i) grating efficiency, ±5% (Table 3); (ii) silicon diode sensitivity, excluding the aperture factor, ±5% (Subsection 6.A); and (iii) silicon diode geometric aperture factor, ±10%. The power spectrum is not well fit by a single temperature Planckian but requires a two-component model consisting of a large plasma area at low temperature (kT ~100 eV) and a comparatively small plasma area at high temperature (kT ~250 eV). This high temperature tail is in qualitative agreement with 2-D radiation magnetohydrodynamic pinch simulation results.[19] Each of the two plasma components contributes a nearly equal amount to the radiated power at the peak emission time of ~7.5 ns. Note that the temperature and area affect the power in combination (i.e., a higher temperature fit and a lower area fit can produce the same total power). Therefore, one must be cautioned that, depending on the noise level of the spectrum that constrains the balance between these two effects, one can see high-frequency swings in the individual terms that do not represent physical changes to the plasma. The total radiated energy of ~900 kJ from the TGS unfold is consistent with independent total energy measurements made by a bolometer diagnostic viewing the same fraction of the Z pinch (863 ± 56 kJ); however, this redundancy is secondary to the primary goal of the TGS in providing

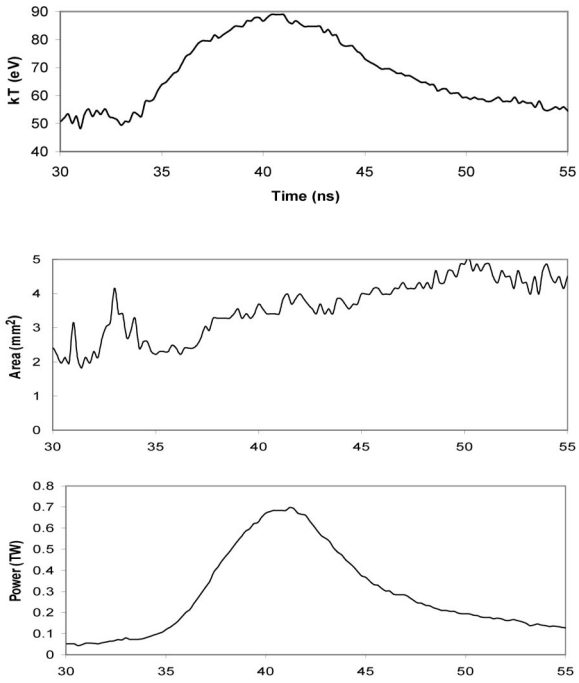

Fig. 33. Temporal history of the hohlraum from experiment Z998. Multiply vertical scale of the power history by a factor of $(1/\pi)/\cos(29°)/\cos(12°) \sim 0.37$ for a Lambertian emitter and by $2/\pi$ for an isotropic emitter. Energy radiated from the viewed area of the Lambertian hohlraum wall is thus ~4 kJ. The horizontal time scale is relative.

spectroscopic information, in this case demonstrating the presence of two temperature components.

2. *Low-Energy TGS17*

This spectrograph employs grating X27 (with the calibration of Fig. 22) and is used as a low-energy diagnostic of pinch-driven hohlraums. The pinch–grating distance is 8.247 m, and the grating–detector distance is 0.607 m. A gold-wall cylinder is centered on and surrounds the cylindrical pinch. To prevent the TGS from viewing the pinch directly, the l-o-s is defined by a small hole in the gold wall. This results in the spectrometer viewing a small (locally plane) section of the inner gold-wall cylinder at an angle of $\theta = 29°$ within the plane of curvature (horizontal). In addition, the l-o-s is also inclined at an angle of $\rho = 12°$ above this horizontal plane. Figures 32 and 33 are the reduced results for one such hohlraum measurement. We find that these sources are well fit by a single-temperature (i.e., thermalized) blackbody, suggesting a higher level of radiation homogeneity than demonstrated above for the direct Z pinch, as expected for a hohlraum wall. The error bars for individual data points are set to $\pm 20\%$ as explained above. As flat-fielding data was not available for this spectrograph, the aperture factor in Eq. (38) was set to 1.

7. Summary

We have presented a new analytical model, derived rigorously from scalar diffraction theory, for the efficiency of a symmetric profile transmission grating. This model arose from the failure of classical rectangular bar calculations to agree with accurate soft-x-ray (0.1–2 keV) measurements of gold gratings. The measurements employed a new table-top calibration system that selects numerous (>30) photon energies by use of a high-resolution grazing-incidence monochromator and a constant current e-beam source equipped with an extensive set of anodes. Beginning with a trapezoidal fit, iterative computations determined the free-form (multiple step) profile that fits all measured spectral orders (1–8) simultaneously. The result is a physically consistent bar-profile model that agrees with the data to within ~1% of the net soft-x-ray efficiency. With this method, fine-period (200 nm) free-standing gratings were found to exhibit limited performance fundamentals despite four generations of refinement:

(i) Because of the nearly equal widths of the bars and intervening spaces, low second-order contamination is obtained over part of the spectrum at the expense of reduced first-order efficiency above ~1 keV and increased scatter.

(ii) Model-inferred physical structures, including organic residue and metal particulates on the gold bars, are verified with electron microscopy and x-ray spectroscopy on a grating physically sectioned after the soft-x-ray calibration.

(iii) The calibrated bar thickness is highly discrepant (±factor 2) from and typically lower than the manufacturers' specifications.

Such variations mandate soft-x-ray testing as a routine nondestructive method to determine the parameters of individual gratings. Selected gratings and fast diodes were used to construct 0.25-ns time-resolved spectrographs of known radiometric response. The unfolded spectra of a direct Z-pinch plasma yielded a peak $kT \sim 250$ eV with a total radiated energy ~900 kJ. A pinch-driven gold-wall hohlraum yielded a thermalized (Planckian) $kT \sim 86$ eV. Such absolutely calibrated diagnostics are important steps on the path to inertial confinement fusion with a Z pinch.

The soft-x-ray efficiency calibration system we have developed provides a spectral resolution sufficient to map photoabsorption edges. With a varied-line-space monochromator,[7] the system was able to select wavelength at high spectral resolution and throughput while maintaining a stationary light source and exit slit. The resulting physical stability of the system provided a temporally stable and reproducible intensity of radiation. Construction of a library of anode materials for an electron-impact light source allowed access to a large number of bright soft-x-ray emission lines at finely spaced intervals between ~0.1 and 2 KeV. Use of a low-noise back-illuminated CCD further provided for temporal stability of the data through long duration exposures. As an option to be considered in future work, Bremsstrahlung continua from high-z anodes (e.g., W or Au)

could also be utilized, provided that the CCD is operated in photon-counting mode to allow separation of monochromator spectral orders and also that of nonmonochromatic scattered radiation by use of the electron gain inherent to a constant work function (electrons per electron volt) of silicon.[24] This use would make continuum measurements of efficiency possible, which is of particular importance in the characterization of the fine spectral structures evident from our research (see Section 5). These structures occur in the vicinity of soft-x-ray photoabsorption edges, not only from the gold grating bar (*M*-shell and *N*-shell) but also from the nickel support structure (*L*-shell) and from organic contaminants (the carbon and oxygen *K*-shell edges, including inverted and cusp-shaped edges demonstrated in the even spectral orders). The table-top soft-x-ray calibration system developed in this work[7] represents a convenient and low-cost alternative to relatively inaccessible and expensive synchrotron radiation facilities and has higher temporal and spatial stability (and lower cost) than currently attainable with laser-produced plasma (pulsed) light sources.

To fit the increasingly accurate and detailed data resulting from these extended soft-x-ray measurement capabilities required new analytical solutions to the absolute efficiencies of symmetric profile transmission gratings. Employing rigorous scalar theory derivation of both linear (trapezoidal and hexagonal) and nonlinear (free-form multiple step) side-wall grating bars and by use of simple models that account for the practical effects of a support structure and contamination, an iterative FORTRAN code was developed that yields high-accuracy fits to the measured soft-x-ray data with the same (physically consistent) model for all spectral orders. An absorption edge at Ni–K also allows the code to determine the physical parameters of a translucent nickel support structure, and a low-energy rise in the second-order efficiencies (including an inverted absorption edge at C–K) determines the concentration of a carbon-based film on the side walls of the gold bars.

The new soft-x-ray measurement system and model were applied to the calibration of the most recent free-standing fine-period transmission gratings available. The large deviation of critical parameters (such as bar thickness and scatter) found between individual gratings highlights the need to accurately measure soft-x-ray efficiencies rather than to assume parameters targeted in the grating fabrication. Indeed, several generations of results reported here were provided as a courtesy to one grating manufacturer (MIT Space Nanostructures Laboratory[13]) and thereby used to improve their fabrication. Such soft-x-ray measurements were needed to obtain accurate knowledge of important physical parameters such as gold-bar or contaminant layer thicknesses otherwise unavailable during the wafer processing. These measurements provide a nondestructive process, whereby acceptable gratings are selected on the basis of their soft-x-ray performance and model-inferred structure.

Transmission gratings of comparatively high performance were selected by the above process, absolutely calibrated, and used to construct time-resolved spectrographs. These instruments were successfully fielded to diagnose *Z*-pinch plasmas from tungsten wire arrays and gold-wall hohlraums driven by emission from such plasmas. Radiometrically calibrated temperatures, areas, and emitted powers from these sources agree with theoretical models and independent experimental measurements.

Theoretically, an amplitude transmission grating consisting of opaque rectangular profile bars and equal width spaces can deliver an ideal flat efficiency as a function of photon energy. However, our results demonstrate that much less ideal characteristics are at present available with such devices, for various reasons:

1. The thickest gold bars that currently can be fabricated on a 200-nm period are sufficiently translucent that phase shifts in the transmitted beam produce large interference bumps near the soft-x-ray gold *M*- and *N*-shell transitions.
2. The wavelength-dependent transmission through the sloped side walls of actual (nonrectangular profile) bars results in a variable bar-to-gap ratio, which prevents the suppression of second-order contamination across a broad spectral range.
3. The need for a rigid grid support structure (e.g., nickel) superimposes onto the spectrum an additional photoabsorption edge as well as a spatial modulation of the efficiency across the grating aperture.
4. The absence of a solid mounting base for free-standing gratings can significantly reduce the presence of absorption edges in the spectral efficiency curves. However, the difficulty of completely removing plating layers needed in the multistep fabrication process often introduces a high level of spectral background owing to the effect of particulate metal (e.g., nickel) contaminants. The fabrication process also reintroduces the photoabsorption edges of carbon and oxygen owing to photoresist or other carbon-based residue on the side walls of the bars. In an attempt to reduce these contaminants, the most recent series of gratings was apparently etched more thoroughly, but resulted in thin, gold grating bars having reduced efficiency at high energies.
5. The presence of residual photoresist on the grating is a potential source of spontaneous degradation of calibration accuracy, because of the possibility of further oxide growth or vacuum contaminants accumulating on the organic films.
6. The free-standing grating structure, even with a robust grid support structure, consists of bars whose deviation from periodicity (including bent bars and high-frequency width and thickness modulations) gives rise to a spectrum contaminated by significant scatter in the form of interorder bumps, shoulders, and high background.
7. The use of such a grating at normal incidence exposes it to severe heat loading and debris contam-

ination from the source, which can result in distortion of the structure and efficiency of the device. Because of the high calibration accuracy of our measurements and model, we have tracked nanometer-sized changes in the effective bar shape after illumination of a grating by a high peak power *Z*-pinch source, inferred from a significant (30%) change in the second-order grating efficiencies.

These practical disadvantages of a free-standing transmission grating and its inherent disadvantages of a lower peak efficiency and dispersive power must be weighed against its advantages in comparison with existing grazing-incidence reflection gratings. These include a higher purity in a broad first-order efficiency curve (i.e., lower efficiency in spectral orders $m > 1$) and in the insensitivity of the efficiency and dispersion of a normal-incidence transmission grating to angular alignment errors. Future work is motivated by the need to develop spectroscopic instruments that can, in practice, exhibit a wider range of desirable features than existing mountings of either free-standing transmission gratings or reflection gratings.

The authors acknowledge helpful discussions with Gordon Chandler and microalignment and interconnection by Kenneth A. Peterson and Rose M. Torres on the test diodes used to calibrate the oxide layer thickness. Sandia is a multiprogram laboratory operated by Sandia Corporation, a Lockheed Martin Company, for the U.S. Department of Energy's National Nuclear Security Administration under contract DE-AC04-94AL85000.

References

1. H. W. Schnopper, L. P. Van Speybroek, J. P. Delvaille, A. Epstein, E. Kallne, R. Z. Bachrach, J. H. Dijkstra, and L. Lantward, "Diffraction grating transmission efficiencies for XUV and soft-x-rays," Appl. Opt. **16,** 1088–1091 (1977).
2. K. Eidmann, M. Kuhne, P. Muller, and G. D. Tsakiris, "Characterization of pinhole transmission gratings," J. X-Ray Sci. Technol. **2,** 259–273 (1990).
3. L. E. Ruggles, M. E. Cuneo, J. L. Porter, D. F. Wenger, and W. W. Simpson, "Measurement of the efficiency of gold transmission gratings in 100–5000 eV photon energy range," Rev. Sci. Instrum. **72,** 1–5 (2001).
4. H. Brauninger, P. Predehl, and K. P. Beuermann, "Transmission grating efficiencies for wavelengths between 5.4 A and 44.8 A," Appl. Opt. **18,** 368–373 (1979).
5. K. A. Flanagan, T. H. Markert, J. E. Davis, M. L. Shattenburg, R. L. Blake, F. Scholze, P. Bulicke, R. Fliegauf, S. Kraft, G. Ulm, and E. M. Gullikson, "Modeling the Chandra high energy transmission gratings below 2 keV," Proc. SPIE **414,** 559–572 (2000).
6. Austin Instruments, Inc., 10 Temple Street, Reading, Mass. 01867-2830, www.austinst.com.
7. Hettrick Scientific, 1-39-59 Tama-cho, Fuchu-shi Tokyo 183-0002 Japan, hettrickscientific@yahoo.com, mhettrick@hotmail.com.
8. M. C. Hettrick, "Surface normal rotation: a new technique for grazing-incidence monochromators," Appl. Opt. **31,** 7174–7178 (1992).
9. M. C. Hettrick, "Grating monochromators and spectrometers based on surface normal rotation," U.S. patent 5,274,435 (28 December 1993).
10. M. C. Hettrick, "Optical design and experimental development of grazing incidence fixed slit spectrometers for high resolution plasma diagnostics," Ph.D. dissertation (The Graduate University for Advanced Studies, Nagoya University, Japan, 1996).
11. LeBow Co., 5960 Mandarin Avenue, Goleta, Calif. 93117, www.lebowcompany.com.
12. Roper Scientific, 3660 Quakerbridge Road, Trenton, N.J. 08619, www.roperscientific.com.
13. M. L. Shattenburg, E. H. Anderson, and H. I. Smith, "X-ray/VUV transmission gratings for astrophysical and laboratory applications," Phys. Scr. **41,** 13–20 (1990).
14. Heidenhain GmbH, Traunreut Germany.
15. B. Henke, P. Lee, T. J. Tanaka, R. L. Shimabukuro, and B. K. Fujikawa, "Low-energy x-ray interaction coefficients: photoabsorption, scattering and reflection," At. Data Nucl. Data Tables **27,** 1 (1982); on-line version at www-cxro.lbl.gov/optical_constants/.
16. E. E. Scime, E. H. Anderson, D. J. McComas, and M. L. Schattenburg, "Extreme-ultraviolet polarization and filtering with gold transmission gratings," Appl. Opt. **34,** 648–654 (1995).
17. S. Sailaja, P. A. Naik, V. Arora, and P. D. Gupta, "Occurrence of half-integral diffraction orders in XUV-soft x-ray spectra using a free-standing transmission grating," J. X-Ray Sci. Technol. **8,** 231–239 (2000).
18. M. K. Matzen, "Z-pinches as intense x-ray sources for high-energy density physics applications," Phys. Plasmas **4,** 1519–1527 (1997).
19. M. E. Cuneo, R. A. Vesey, J. L. Porter, Jr., G. A. Chandler, D. L. Fehl, T. L. Gilliland, D. L. Hanson, J. S. McGurn, P. G. Reynolds, L. E. Ruggles, H. Seamen, R. B. Spielman, K. W. Struve, W. A. Styger, W. W. Simpson, J. A. Torres, and D. A. Wenger, "Development and characterization of a Z-pinch-driven hohlraum high-yield inertial confinement fusion target concept," Phys. Plasmas **8,** 2257–2267 (2001).
20. M. E. Cuneo, R. A. Vesey, J. L. Porter, Jr., G. R. Bennett, D. L. Hanson, L. E. Ruggles, W. W. Simpson, G. C. Idzorek, W. A. Stygar, J. H. Hammer, J. J. Seamen, J. A. Torres, J. S. McGurn, and R. M. Green, "Double Z-pinch hohlraum drive with excellent temperature balance for symmetric inertial confinement fusion capsule implosions," Phys. Rev. Lett. **88,** 215004, 1–4 (2002).
21. International Radiation Detectors Inc., 2527 West 237th Street, Unit C, Torrance Calif. 90505-5243, www.ird-inc.com.
22. J. F. Seely, C. N. Boyer, G. E. Holland, and J. L. Weaver, "X-ray absolute calibration of the time response of a silicon photodiode," Appl. Opt. **41,** 5209–5217 (2002).
23. J. L. Weaver, G. Holland, U. Feldman, J. F. Seely, C. M. Brown, V. Serlin, A. V. Deniz, and M. Klapisch, "The determination of absolutely calibrated spectra from laser produced plasmas using a transmission grating spectrometer at the Nike laser facility," Rev. Sci. Instrum. **72,** 108–118 (2001).
24. K. C. Gendreau, M. D. Audley, K. A. Arnaud, K. R. Boyce, R. Fujimoto, Y. Ishisaki, R. L. Kelley, T. Mihara, K. Mitsuda, F. S. Porter, C. K. Stahle, and A. E. Szymkowiak, "ASTRO-E/XRS calibration program and results," in *EUV, X-Ray, and Gamma-Ray Instrumentation for Astronomy X*, O. H. Siegmund and K. A. Flanagan, eds., Proc. SPIE **3765,** 137–147 (1999).